Plant, Cell & Environment

Plant, Cell and Environment (2014) **37**, 1516–1535 doi: 10.1111/pce.12262

Original Article

Carbon isotope discrimination during branch photosynthesis of *Fagus sylvatica*: a Bayesian modelling approach

Lydia Gentsch[1,2], Albin Hammerle[1,3], Patrick Sturm[1,4], Jérôme Ogée[2], Lisa Wingate[2], Rolf Siegwolf[5], Peter Plüss[1], Thomas Baur[1], Nina Buchmann[1] & Alexander Knohl[1,6]

[1]*Institute of Agricultural Sciences, ETH Zurich, Universitätsstrasse 2, Zurich 8092, Switzerland,* [2]*UR1263 Ephyse, INRA, Villenave d'Ornon 33140 France,* [3]*Institute of Ecology, University of Innsbruck, Sternwartestrasse 15, Innsbruck 6020, Austria,* [4]*Tofwerk AG, Uttigenstrasse 22, Thun 3600, Switzerland,* [5]*Laboratory for Atmospheric Chemistry/Stable Isotopes and Ecosystem Fluxes, PSI – Paul Scherrer Institute, Villigen 5232, Switzerland and* [6]*Chair of Bioclimatology, Georg-August University of Göttingen, Büsgenweg 2, Göttingen 37077, Germany*

ABSTRACT

Field measurements of photosynthetic carbon isotope discrimination ($^{13}\Delta$) of *Fagus sylvatica*, conducted with branch bags and laser spectrometry, revealed a high variability of $^{13}\Delta$, both on diurnal and day-to-day timescales. We tested the prediction capability of three versions of a commonly used model for $^{13}\Delta$ [called here comprehensive ($^{13}\Delta_{comp}$), simplified ($^{13}\Delta_{simple}$) and revised ($^{13}\Delta_{revised}$) versions]. A Bayesian approach was used to calibrate major model parameters. Constrained estimates were found for the fractionation during CO_2 fixation in $^{13}\Delta_{comp}$, but not in $^{13}\Delta_{simple}$, and partially for the mesophyll conductance for CO_2 (g_i). No constrained estimates were found for fractionations during mitochondrial and photorespiration, and for a diurnally variable apparent fractionation between current assimilates and mitochondrial respiration, specific to $^{13}\Delta_{revised}$. A quantification of parameter estimation uncertainties and interdependencies further helped explore model structure and behaviour. We found that $^{13}\Delta_{comp}$ usually outperformed $^{13}\Delta_{simple}$ because of the explicit consideration of g_i and the photorespiratory fractionation in $^{13}\Delta_{comp}$ that enabled a better description of the large observed diurnal variation (≈9‰) of $^{13}\Delta$. Flux-weighted daily means of $^{13}\Delta$ were also better predicted with $^{13}\Delta_{comp}$ than with $^{13}\Delta_{simple}$.

Key-words: Farquhar model; gas exchange; isotopologues; laser spectrometer; open branch bags; photosynthetic ^{13}C discrimination.

INTRODUCTION

The widespread use of stable carbon isotopes as a tool in biogeochemical research generally requires a reliable prediction of carbon isotope discrimination by plant photosynthesis ($^{13}\Delta$) at various temporal and spatial scales (Werner *et al.* 2012). This is highlighted in isotope-constrained global carbon budgets, where small changes in $^{13}\Delta$ (<1‰) at the continental scale can result in significant uncertainties in the partitioning of net CO_2 fluxes between the terrestrial biosphere and the ocean (e.g. Randerson 2002; Ballantyne *et al.* 2010). An accurate prediction of $^{13}\Delta$ is further necessary for isotope-based partitioning of the net ecosystem CO_2 exchange (e.g. Bowling *et al.* 2001; Ogée *et al.* 2003; Knohl & Buchmann 2005; Zobitz *et al.* 2008) and the inference of canopy photosynthetic gas exchange from $^{13}C/^{12}C$ ratios of respired CO_2 (e.g. Ekblad *et al.* 2005; Knohl & Buchmann 2005; Knohl *et al.* 2005) or phloem sugars (e.g. Keitel *et al.* 2003; Ubierna & Marshall 2011). This is especially important as post-photosynthetic fractionations during biomass formation and respiration are known to alter the original isotopic imprint of $^{13}\Delta$ on plant-derived organic matter and respired CO_2 (e.g. Tcherkez *et al.* 2011a; Werner & Gessler 2011). Assigning the observed variability of $^{13}C/^{12}C$ ratios of organic matter or respired CO_2 to the proper metabolic process (photosynthesis, plant internal metabolism, respiration) is thus necessary for deciphering and using the environmental information contained in $^{13}C/^{12}C$ ratios.

The most commonly used model for predicting $^{13}\Delta$ in C_3 plants was developed by Farquhar *et al.* (1982), and recently updated for ternary effects in leaf gas exchange (Farquhar & Cernusak 2012). Often, a simplified version of this model ($^{13}\Delta_{simple}$) is used (e.g. Farquhar *et al.* 1982; Bowling *et al.* 2001; Betson *et al.* 2007; Michelot *et al.* 2011) that only accounts for the two largest isotope fractionations during stomatal diffusion and CO_2 fixation (see Eqn 5). However, field studies with direct measurements of $^{13}\Delta$ (called $^{13}\Delta_{obs}$ hereafter) have shown that the natural variability of $^{13}\Delta_{obs}$ is often (Wingate *et al.* 2007; Bickford *et al.* 2009, 2010) but not always (Bickford *et al.* 2009, 2010) better predicted by a more comprehensive version of the model ($^{13}\Delta_{comp}$) that accounts for the whole chain of resistances towards the CO_2 drawdown to the carboxylation sites and for fractionations during mitochondrial and photorespiration (see Eqn 3 below). For predictions of $^{13}\Delta$ at canopy and global scales both $^{13}\Delta_{simple}$

Correspondence: L. Gentsch. e-mail: lydia.gentsch@bordeaux.inra.fr

(e.g. Baldocchi & Bowling 2003; Chen & Chen 2007; Ballantyne *et al*. 2011) and $^{13}\Delta_{comp}$ (e.g. Ogée *et al*. 2003; Suits 2005; Cai *et al*. 2008) are currently used, but fractionation during mitochondrial respiration is usually neglected. A field study on *Picea sitchensis* (Bong.) Carr. (Wingate *et al*. 2007) reported high $^{13}\Delta_{obs}$ values that were not explained by $^{13}\Delta_{comp}$. The authors suggested that this mismatch resulted from isotopic disequilibria caused by a difference in the $^{13}C/^{12}C$ ratios of current assimilates and the actual substrates fuelling mitochondrial respiration in the light (R_{day}). To achieve a quantitative description of such offsets, a diurnally variable apparent isotope fractionation factor (e*) was added ($^{13}\Delta_{revised}$; see Eqn 4 below). Recent evidence supports this view and suggests that R_{day} is generally fuelled by older carbon pools that are likely ^{13}C-enriched compared with current assimilates (Tcherkez *et al*. 2010, 2011b).

Despite the insights from earlier field studies (Harwood *et al*. 1998; Wingate *et al*. 2007; Bickford *et al*. 2009, 2010), we are currently missing thorough field-based evaluations of the available $^{13}\Delta$ models on longer datasets that encompass both diurnal and seasonal variabilities of $^{13}\Delta_{obs}$ (Wingate *et al*. 2010). Here, we use a 60-day-long dataset of continuous (sub-hourly) $^{13}\Delta_{obs}$ measurements on leafy branches of mature European beech (*Fagus sylvatica* (L.)) trees and test the prediction capabilities of the different $^{13}\Delta$ model versions outlined above. Continuous measurements of $^{13}\Delta_{obs}$ were made possible through the deployment of a laser spectrometer for CO_2 isotopologue concentration measurements (QCLAS-ISO; Aerodyne Research Inc., Billerica, MA, USA) and three automated open branch bags.

Model calibrations of $^{13}\Delta_{simple}$, $^{13}\Delta_{comp}$ and $^{13}\Delta_{revised}$ are accomplished using a Bayesian inversion scheme. Model performances are explored by investigating mean diurnal patterns and the day-to-day variability of flux-weighted daily means for observed and predicted $^{13}\Delta$. The Bayesian model calibration approach enabled a sound treatment of uncertainties, originating from model structure, parametrization and $^{13}\Delta_{obs}$ measurement error. It thereby helped to evaluate the amount of model-relevant information contained in our $^{13}\Delta_{obs}$ data. Consequently, we obtained insights from the Bayesian model calibration on parameter interdependencies and their influence on parameter estimation and constraint. We also show examples from an additional sensitivity analysis for single model parameters. Finally, we use the calibrated $^{13}\Delta_{simple}$ and $^{13}\Delta_{comp}$ models to explore the overall importance of single model terms over the diurnal cycle.

MATERIALS AND METHODS

Field site and measurement trees

The Lägeren research site is located on a south-facing mountain slope at 682 a.s.l and 20 km north-west of Zurich in Switzerland. Vegetation is a mixed deciduous forest dominated by European beech (*F. sylvatica* (L.)) and dominant trees are about 31 m high (Eugster *et al*. 2007). In 2010, mean annual air temperature was 7.7 °C and annual precipitation was 888 mm (BAFU 2011). Three co-dominant beech trees, 17 to 20 m high, were each equipped with a gas exchange measurement chamber (branch bag). Branch bags (replicates called BB1, BB2 and BB3 hereafter) were installed at about 2 m height. To compensate for the low height in the canopy, the selected branches were situated upslope of a windthrow area with a southern or south-eastern orientation in order to ensure full or partial exposure to direct sunlight. The distance between trees was 5 to 20 m.

Field set-up and branch bags

The branch bags were connected to a set of laser spectrometers for CO_2 (QCLAS-ISO; Aerodyne Research Inc., Billerica, MA, USA) and water vapour (WVIA; Los Gatos Research Inc., Mountain View, CA, USA) isotopologue concentration measurements, located in an air-conditioned hut. Each branch bag was measured every 45 min. Branch bags and laser spectrometers were connected by polytetrafluoroethylene (PTFE) tubing, heated at 15 °C above ambient temperature. The branch bags had a volume of 69 dm^3 and enclosed between 110 to 250 leaves. The construction frame consisted of two elliptical plexiglass end pieces, connected by aluminium rods, and was covered with a highly transparent, 50 μm thin FEP film (Norton® FEP-WF; Saint-Gobain, Willich, Germany). Between measurements and a 30 min steady-state establishment period, the branch bag air volume was flushed thoroughly. Steady-state conditions were established with a blowing axial fan (D481T-024KA-3; Micronel AG, Tagelswangen, Switzerland), set to a variable flow rate (9 to 60 dm^3 min^{-1}) controlled by an air mass flow sensor (AWM 720P1, Honeywell Sensing and Control, Golden Valley, MN, USA) and dependent on the incident photosynthetic active radiation (PAR) 30 min prior to measurements. A valve-switching system mediated subsampling of ambient (inlet) and chamber (outlet) air. For a particular branch bag sampling, two inlet measurements (lasting 80 s) were carried out before and after one outlet measurement (lasting 110 s). The laser spectrometers operated at 1 Hz and measurements were averaged to a 5 s logging interval. All branch bags were equipped with a sensor for PAR (SQ-110; Apogee Instruments Inc., Logan, UT, USA), a combined sensor for air temperature and relative humidity (HygroClip S3–C03; Rotronic AG, Bassersdorf, Switzerland) and two thermocouples for measuring leaf temperature (PTFE-coated Thermocouple Type T 0.08 mm; Omega Engineering Inc., Stamford, CT, USA), each attached to the lower sides of two different leaves (Table 1). Duplicate air temperature measurements were further made in two out of three branch bags using thermocouples (Thermocouple Type T 0.2 mm, TC-Direct, Mönchengladbach, Germany). A calibration routine for the laser spectrometers was conducted every 90 min, with standard gases referenced to the WMO scale for CO_2 mixing ratios and the V-PDB-CO_2 scale for the isotope ratios (Kaiser 2008). The campaign-long instrument stability for calibrated measurements of the CO_2 mole fraction, δ^{13}C and δ^{18}O was ±0.22 ppm, ±0.21‰ and ±0.21‰, respectively. Details for the QCLAS-ISO and WVIA instrument set-ups can be found in Sturm *et al*. (2012) and in Sturm & Knohl (2010), respectively.

Table 1. List of abbreviations used in the text

Abbreviation	Definition	Unit
A_n	Measured rate of branch net CO_2 assimilation	μmol m^{-2} s^{-1}
BB1 to 3	Branch bag number	
a	^{13}C fractionation during CO_2 diffusion through the stomata (4.4‰)	‰
a_b	^{13}C fractionation during CO_2 diffusion across the leaf boundary layer (2.9‰)	‰
a_l	^{13}C fractionation during diffusion of dissolved CO_2 in the liquid phase (0.7‰)	‰
$\bar{a}$	Weighted ^{13}C fractionation during CO_2 diffusion across the leaf boundary layer and through the stomata in series	‰
α_{ac}	^{13}C fractionation factor for the isotopologues of CO_2 diffusing in air	
α_b	^{13}C fractionation factor for carboxylations in C_3 plants	
α_f	^{13}C fractionation factor for photorespiratory decarboxylation	
α_e	^{13}C fractionation factor for mitochondrial respiratory decarboxylation	
b	Net ^{13}C discrimination during carboxylations by Ribulose 1.5-bisphosphate carboxylase/oxygenase and Phosphoenolpyruvate carboxylase in C_3 plants	‰
$\bar{b}$	Net ^{13}C discrimination during carboxylations in C_3 plants in $^{13}\Delta_{simple}$ only, adjusted to account for omitted CO_2 transfer resistances	‰
$c_a = c_o$	CO_2 mole fraction in dry branch bag air	μmol mol^{-1}
c_e	CO_2 mole fraction in dry ambient air outside the branch bags	μmol mol^{-1}
c_c	CO_2 mole fraction at the carboxylation sites	μmol mol^{-1}
c_i	CO_2 mole fraction in the intercellular spaces	μmol mol^{-1}
c_s	CO_2 mole fraction in dry air at the leaf surface	μmol mol^{-1}
δ_e	Carbon isotope ratio of dry ambient air outside the branch bags	‰
δ_o	Carbon isotope ratio of dry branch bag air	‰
$^{13}\Delta_{obs}$	Observed net ^{13}C discrimination during branch photosynthesis (Eqn 1)	‰
$^{13}\Delta_{simple}$	Predicted net ^{13}C discrimination during branch photosynthesis (Eqn 5)	‰
$^{13}\Delta_{comp}$	Predicted net ^{13}C discrimination during branch photosynthesis (Eqn 3)	‰
$^{13}\Delta_{revised}$	Predicted net ^{13}C discrimination during branch photosynthesis (Eqn 4)	‰
$^{13}\Delta_{x,H}$	Hour of day means of observed or predicted $^{13}\Delta_x$ for all field campaign data. Hours relate to the subsequent hour (CET).	‰
$^{13}\Delta_{x,D}$	Flux (A_n)-weighted daily means of observed or predicted $^{13}\Delta_x$	‰
e	^{13}C fractionation during mitochondrial respiratory decarboxylation	‰
e^*	Apparent ^{13}C fractionation associated with R_{day} if fuelled from older substrates	‰
e_s	^{13}C fractionation during equilibrium dissolution of CO_2 into the liquid phase (1.1‰)	‰
f	^{13}C fractionation during photorespiratory decarboxylation	‰
g_b	Branch boundary-layer conductance to CO_2	mol m^{-2} s^{-1}
g_i	Estimated internal (mesophyll) conductance to CO_2	mol m^{-2} s^{-1}
$g_{s,\ obs}$	Observed branch stomatal conductance to CO_2	mol m^{-2} s^{-1}
$g_{s,\ mod}$	Predicted branch stomatal conductance to CO_2 (Eqn 2)	mol m^{-2} s^{-1}
Γ^*	T_{leaf}-dependent CO_2 compensation point in the absence of R_{day} (Eqn 7)	μmol mol^{-1}
k	Carboxylation efficiency (Eqn 9)	mol m^{-2} s^{-1}
MLE	Maximum likelihood estimates for calibrated model parameters	
PAR	Measured photosynthetic active radiation	μmol m^{-2} s^{-1}
R_{day}	Branch respiration during the day, predicted as a function of R_{night} and T_{leaf} (Eqn 8)	μmol m^{-2} s^{-1}
R_{night}	Measured branch respiration during the night	μmol m^{-2} s^{-1}
h	Observed relative humidity (calculated from WVIA water vapour measurements)	%
RMSE	Root mean square error	
T_{leaf}	Measured lower leaf surface temperature in the branch bag	°C
$Y_{2.5}$ and $Y_{97.5}$	2.5 and 97.5 percentiles of the model predictive uncertainty for each $^{13}\Delta$ prediction	‰

Data handling and dataset

Data processing and statistical analysis were done using R 2.9.2 (R Development Core Team 2009) and MATLAB (The MathWorks Inc., Natick, MA, USA). Photosynthetic ^{13}C discrimination was only calculated if PAR was greater than 10 μmol m^{-2} s^{-1}. Measurements with a high inlet or outlet variability, an inlet-to-outlet CO_2 drawdown less than 10 ppm or a standard deviation (SD) for $^{13}\Delta_{obs}$ greater than 6‰ were discarded. The SD of $^{13}\Delta_{obs}$ was calculated from the SD of inlet and outlet measurements using Gaussian error propagation (Taylor 1997).

Calculation of $^{13}\Delta_{obs}$

The observed net carbon isotope discrimination during photosynthesis of leafy branches ($^{13}\Delta_{obs}$) was calculated from QCLAS-ISO measured CO_2 mole fractions and isotope compositions of dry air at branch bag inlets (c_e, δ_e) and outlets (c_o, δ_o) at steady-state conditions, following Evans *et al.* (1986):

$$^{13}\Delta_{obs} = \frac{\xi(\delta_o - \delta_e)}{1 + \delta_o - \xi(\delta_o - \delta_e)} \quad \text{with} \quad \xi = \frac{c_e}{c_e - c_o} \tag{1}$$

Further gas exchange related calculations are given in the Appendix.

Estimation of boundary-layer and stomatal conductances

The one-sided boundary-layer conductance inside each branch bag (g_b) was approximated from leaf heat transfer estimates using average leaf dimensions and wind speed measurements (ThermoAir2, Schiltknecht, Gossau, Switzerland) above leaf surfaces during varying flow rates, following Jones (1992). Using an average measured wind speed of 0.4 m s^{-1} and leaf widths ranging from 36 to 42 mm, the one-sided boundary-layer conductance for CO_2 during the day ranged from 0.74 to 0.80 mol m^{-2} s^{-1}, depending on the branch bag considered.

Two different approaches were used to obtain estimates of stomatal conductance (g_s). In the first approach, g_s was calculated directly from water vapour measurements as described in the appendix. These observed g_s values (called $g_{s,obs}$ hereafter) were used for model calibrations and predictions only if they had passed several data quality filters to remove (1) potential water vapour condensation events within the branch bags, (2) high standard deviations (>5% of the mean) for inlet or outlet water vapour measurements and (3) large differences (>1 °C) between the duplicate leaf temperature measurements within each branch bag. This data quality filtering for $g_{s,obs}$ resulted in the retention of 50 to 65% of the $^{13}\Delta_{obs}$ data, depending on the branch bag. Data loss was more pronounced for midday measurements than for other times of the day because of effects from higher transpiration rates (filter 1), greater inlet variabilities (filter 2) and a greater probability of heterogeneous leaf temperatures (filter 3) during midday. Higher transpiration rates during midday made measurements more susceptible to condensation in the non-frequent case of non-optimal tuning of the flow rate through the branch bag (e.g. caused by quick changes from cloudy to sunny conditions).

Because we wanted to retain 100% of the $^{13}\Delta_{obs}$ data, we also used a second approach where stomatal conductance was modelled ($g_{s,mod}$) from observed gas exchange parameters, using a simple version of the Ball–Berry model (Collatz *et al.* 1991):

$$g_{sc} = m\frac{A_n\, h_s}{c_s} + n \tag{2}$$

where g_{sc} is the stomatal conductance for CO_2, A_n is the net CO_2 assimilation, h_s is the relative humidity of air at the leaf surface, c_s is the CO_2 mole fraction of dry air at the leaf surface and m and n are the slope and intercept of the linear model. Linear regression analysis was done separately for each branch bag, using quality-filtered $g_{s,obs}$ and h_s data. The obtained slopes and intercepts were then used to calculate $g_{s,mod}$ over a dataset with h_s calculated without the water vapour data quality filters and gap filled with relative humidity (h) sensor data for periods with WVIA instrument failure. Linear regression analysis led to $m = 3.0$ and $n = 15$ mmol m^{-2} s^{-1} [$r^2 = 0.28$, root mean square error (RMSE) = 0.026 and $P < 0.0001$] for BB1, $m = 3.0$ and $n = 34$ mmol m^{-2} s^{-1} ($r^2 = 0.23$, RMSE = 0.049 and $P < 0.0001$) for BB2 and $m = 2.7$ and $n = 25$ mmol m^{-2} s^{-1} ($r^2 = 0.15$, RMSE = 0.036 and $P < 0.0001$) for BB3. An analysis of the model residuals indicated no dependencies on model input parameters. A model sensitivity analysis further indicated that A_n ($r^2 > 0.85$) and c_s ($r^2 > 0.6$) were stronger drivers of $g_{s,mod}$ than h_s ($r^2 < 0.45$), fostering robust g_s predictions. We point out that the majority of filtered $g_{s,obs}$ data was not *per se* erroneous (apart from non-detected condensation events), but potentially impaired by issues of measurement precision, likely to originate from heterogeneous g_s for ≈200 leaves and the sensitivity of the g_s calculation to small errors in leaf temperature or other input variables.

Model parametrization

Three different versions of the Farquhar *et al.* (1982) model were used. The comprehensive model ($^{13}\Delta_{comp}$) describes the net $^{13}\Delta$ in C_3 plants as the sum of relatively small, successive ^{13}C discriminations during CO_2 diffusion from the atmosphere to the chloroplast and a large ^{13}C discrimination related to CO_2 fixation, minus the ^{13}C discriminations associated with photorespiration and mitochondrial day respiration:

$$^{13}\Delta_{comp} = a_b\frac{c_a - c_s}{c_a} + a\frac{c_s - c_i}{c_a} + (e_s + a_l)\frac{c_i - c_c}{c_a} + b\frac{c_c}{c_a} - f\frac{\Gamma^*}{c_a} - e\frac{R_{day}}{A_n + R_{day}}\frac{c_c - \Gamma^*}{c_a} \tag{3}$$

where c_a, c_s, c_i and c_c are the CO_2 mole fractions in the chamber surrounding the branch, at the leaf surface, in the intercellular spaces before CO_2 enters into solution and at the sites of carboxylation, respectively, R_{day} is the mitochondrial dark respiration in the light, a_b (2.9‰) and a (4.4‰) are the fractionations associated with CO_2 diffusion through the leaf boundary layer and the stomata, e_s (1.1‰) represents the equilibrium fractionation occurring as CO_2 enters into solution, a_l (0.7‰) is the fractionation associated with diffusion of dissolved CO_2 in the liquid phase, b is the net discrimination occurring during carboxylations in C_3 plants; f is the fractionation occurring during photorespiration (see Farquhar *et al.* 1982; Farquhar & Richards 1984; Farquhar *et al.* 1989 and references therein) and e, the fractionation during R_{day}, designates the offset between the isotope ratios of the current assimilates and R_{day} (Ghashghaie *et al.* 2003; Tcherkez *et al.* 2011b). Wingate *et al.* (2007) extended $^{13}\Delta_{comp}$ by introducing e^*, an apparent fractionation factor for R_{day}, expressing the difference between the isotope ratios of the current assimilates and the respiratory substrate at a given time. It is included into $^{13}\Delta_{comp}$ as follows:

$$^{13}\Delta_{revised} = a_b\frac{c_a - c_s}{c_a} + a\frac{c_s - c_i}{c_a} + (e_s + a_l)\frac{c_i - c_c}{c_a} + b\frac{c_c}{c_a} - f\frac{\Gamma^*}{c_a} - (e + e^*)\frac{R_{day}}{A_n + R_{day}}\frac{c_c - \Gamma^*}{c_a} \tag{4}$$

The most simplified version of the $^{13}\Delta$ model ($^{13}\Delta_{simple}$) neglects the isotope effects associated with CO_2 transfer through the leaf boundary layer as well as photorespiratory and respiratory decarboxylations, and accounts partly for the isotope effects associated with internal CO_2 transfer by using a lower value for b ($\bar{b} \approx 27‰$) (Farquhar & Richards 1984):

$$^{13}\Delta_{simple} = a + (\bar{b} - a)\frac{c_i}{c_a} \tag{5}$$

Recently, Farquhar & Cernusak (2012) introduced correction terms for ternary effects on $^{13}\Delta$ calculations, to be consistent with the commonly applied ternary effect corrections for gas exchange calculations (von Caemmerer & Farquhar 1981). They showed that such corrections were small compared with the situation where no correction was applied to both the gas exchange and $^{13}\Delta$. The impact of ternary corrections on model calibration and behaviour was tested for the $^{13}\Delta_{comp}$ model. Equations including these ternary corrections are given in the appendix (Eqns A14 and A15). However for the most part of this study, we chose not to apply any ternary correction in the gas exchange and $^{13}\Delta$ calculations. CO_2 mole fractions at the leaf surface, in the intercellular spaces and at the sites of carboxylation were then calculated as:

$$c_s = c_a - \frac{A_n}{g_b};\, c_i = c_s - \frac{A_n}{g_{s,}};\, c_c = c_i - \frac{A_n}{g_i} \tag{6}$$

where $g_{b,}$ g_s and g_i denote boundary layer, stomatal and internal conductances to CO_2. For the $^{13}\Delta_{comp}$ model (Eqn 3), we also tested the impact of a leaf temperature dependency of g_i (e.g. Bernacchi *et al.* 2002; Warren & Dreyer 2006; Evans & von Caemmerer 2013) on model calibration and behaviour. In this case, c_c was calculated as

$$c_c = c_i - \frac{A_n}{g_i^{25} * Q_{10}^{\left(\frac{T_{Leaf-25}}{10}\right)}} \tag{7}$$

where T_{leaf} denotes leaf temperature in °C and Q_{10} is assumed to be 2.0 (Bernacchi *et al.* 2002). The CO_2 compensation point in the absence of R_{day} (Γ^*) was modelled as a function of leaf temperature according to Bernacchi *et al.* (2001):

$$\Gamma^* = \Gamma^*_{25°C} \exp\left(\frac{\Delta H_a}{R_m}\left(\frac{1}{298.15} - \frac{1}{T_{leaf,K}}\right)\right) \tag{8}$$

where $\Gamma^*_{25°C}$ is the Γ^* at 25 °C (42.75 μmol mol^{-1}); $T_{leaf,K}$ is the leaf temperature in K; ΔH_a represents the activation energy for photorespiratory processes (37.83 kJ mol^{-1}), and R_m is the ideal gas constant. R_{day} was modelled, using Q_{10} functions derived from exponential fits of nocturnal branch respiration (R_{night}) versus leaf temperature (T_{leaf}) assuming a 50% inhibition (Atkin *et al.* 2005; Tcherkez *et al.* 2005) of R_{day} compared with R_{night}:

$$R_{day} = 0.5\left(R_{ref}\, Q_{10}^{\frac{T_{leaf}-T_{ref}}{10}}\right) \tag{9}$$

where R_{ref} represents R_{night} at a $T_{leaf} = T_{ref}$. Fitted Q_{10} values were 1.92 (BB1), 2.29 (BB2) and 2.05 (BB3).

Model calibration

A Bayesian approach was used for model calibration that had the advantage of providing quantitative measures of uncertainty and correlation among the calibrated parameters, in addition to parameter estimates (Van Oijen *et al.* 2005). The following variables (called model parameters hereafter) was included in this calibration exercise: g_i (or g_i^{25}), b (or $\bar{b}$), f, e and e^*. Initial (*a priori*) values and uncertainties for each parameter were prescribed and used to compute uniform prior probability distributions (uninformative priors). Model calibration was then performed by maximizing the negative logarithm of a likelihood function, that quantifies the probability that the observed data was generated by a particular parameter set of a given model (Schoups & Vrugt 2010). By application of Bayes' theorem, a posterior probability distribution for all parameters was obtained. A Markov Chain Monte Carlo (MCMC) algorithm was used to approximate the posterior probability distribution, by drawing a large representative sample from the parameter space (Van Oijen *et al.* 2005). All computational steps were conducted with the Differential Evolution Adaptive Metropolis (DREAM, version 1.4) algorithm encoded in MATLAB (The MathWorks Inc.) from Vrugt *et al.* (2009). We further computed the so-called model predictive uncertainty using an algorithm introduced by Schoups & Vrugt (2010), that accounts for uncertainties in the measurements, the model input and parameters and the model structure, without separating out the various error sources. In this paper, the model predictive uncertainty is characterized by the 2.5 and 97.5 percentiles.

A priori values for $\bar{b}$, b, f, e and e^* were derived from the literature as follows: 27 ± 1‰ for $\bar{b}$ (Farquhar & Richards 1984; Farquhar *et al.* 1989), 26–30‰ for b (Roeske & O'Leary 1984; Guy *et al.* 1993; McNevin *et al.* 2007; Lanigan *et al.* 2008), 8–12‰ for f (Igamberdiev *et al.* 2004; Tcherkez 2006; Lanigan *et al.* 2008), −6 to 0‰ or not known for e (Ghashghaie *et al.* 2003; Tcherkez *et al.* 2011b), −10 to 0‰ for e^* (Wingate *et al.* 2007). For the calibration of $^{13}\Delta_{revised}$, either g_i, b, f, e and e^* were all estimated simultaneously or only e^* was estimated, while g_i, b, f and e were set to fixed values. Since e^* was expected to vary over the day, the complete $^{13}\Delta_{obs}$ dataset was binned according to the time of the day (leading to 13 subsets spread between 0600 and 1900 h CET) and a different value of e^* was estimated for each time of the day.

Warren *et al.* (2007) reported g_i ranging from 0.14 to 0.24 mol m^{-2} s^{-1} for mature beech trees. Relying on the above *a priori* values for $\bar{b}$, b, f and e, we *a priori* tested that g_i range with our data using both the slope method introduced by Evans *et al.* (1986) and the single point method of Lloyd *et al.* (1992). Both methods rely on the assumptions that $^{13}\Delta$ at infinite g_i ($^{13}\Delta_i$) can be approximated by $^{13}\Delta_{simple}$ (using b instead of $\bar{b}$) and that $^{13}\Delta_{obs}$ is entirely predicted by $^{13}\Delta_{comp}$. Data points with $^{13}\Delta_i < {}^{13}\Delta_{obs}$ were excluded from g_i estimation, as both methods would otherwise lead to unrealistic

g_i values (Bickford *et al.* 2010; Douthe *et al.* 2011). Derived *a priori* values for g_i were in the range of 0.16 to 0.36 mol m^{-2} s^{-1}, consistent with Warren *et al.* (2007), but also suggesting the use of a wider prior parameter uncertainty (0.1 to 0.5 mol m^{-2} s^{-1}) for model calibrations.

We always conducted two parallel model calibrations on each branch bag, using either $g_{s,obs}$ or $g_{s,mod}$ for c_i calculations. As explained above, the stringent data filtering on $g_{s,obs}$ had caused an underrepresentation of midday data. The additional use of modelled g_s ($g_{s,mod}$) allowed a better description of the diurnal patterns (including middays), and thus enabled more representative flux-weighted daily means. The subsequent comparison of the $g_{s,obs}$ and $g_{s,mod}$ approaches allowed us to check the sensitivity of the model calibration to the g_s dataset. In the following, we will only show results using $g_{s,mod}$, but any difference in model parameter estimates and correlations will be discussed explicitly. Predictions of $^{13}\Delta$ from Eqn 3 using either $g_{s,obs}$ or $g_{s,mod}$ are also shown for each single day in the Supporting Information Figs S4 to S13.

RESULTS

Temporal and spatial variability of $^{13}\Delta_{obs}$

Branch bag measurements of $^{13}\Delta_{obs}$ exhibited a high short-term variability with often large differences between two consecutive measurements (Fig. 1). This short-term variability, usually linked to rapid changes in PAR, was however embedded in a regular diurnal time course of $^{13}\Delta_{obs}$, characterized by high $^{13}\Delta_{obs}$ during morning and evening hours and low $^{13}\Delta_{obs}$ at midday. Low $^{13}\Delta_{obs}$ were associated with high net CO_2 assimilation (A_n) and vice versa (data not shown). Spatial or between-tree (BB1 to BB3) variability was also present (Fig. 1e,h,k), but the overall diurnal patterns of $^{13}\Delta_{obs}$ from the three branch bags were fairly consistent. A pronounced day-to-day variability of $^{13}\Delta_{obs}$ was observed as well (Fig. 1d,e,f). It primarily reflected changes in environmental conditions, as illustrated in Fig. 1 for only three diurnals but with very distinctive PAR regimes (mixed, sunny and cloudy).

Model performance of $^{13}\Delta_{simple}$ and $^{13}\Delta_{comp}$

For these three example days both $^{13}\Delta_{simple}$ and $^{13}\Delta_{comp}$ models tracked the short-term variability of $^{13}\Delta_{obs}$ reasonably well (Fig. 1). The model predictive uncertainty (Fig. 1, shaded areas) of both $^{13}\Delta_{simple}$ and $^{13}\Delta_{comp}$ always encompassed $^{13}\Delta_{obs}$ values but was systematically more spread for $^{13}\Delta_{simple}$, especially for BB1, indicating a larger prediction uncertainty of the $^{13}\Delta_{simple}$ model. The quantification of the overall $^{13}\Delta_{simple}$ and $^{13}\Delta_{comp}$ model performances for the entire field campaign (Table 2) showed that $^{13}\Delta_{comp}$ was in general a better predictor of $^{13}\Delta_{obs}$ than $^{13}\Delta_{simple}$. For all 3 branch bags, $^{13}\Delta_{comp}$ showed a higher maximum likelihood and a lower RMSE than $^{13}\Delta_{simple}$ as well as better regression slopes and intercepts (Table 2).

$^{13}\Delta_{simple}$ and $^{13}\Delta_{comp}$ model performances on diurnal timescales

The calculation of hourly means of observed and predicted $^{13}\Delta$ over the entire field campaign (Fig. 2) emphasised the consistent diurnal pattern for $^{13}\Delta_{obs}$ already shown in Fig. 1. This mean diurnal variability of $^{13}\Delta_{obs}$ was well predicted by $^{13}\Delta_{comp}$, while $^{13}\Delta_{simple}$ predicted more damped diurnal variations, irrespective of the values used for the model parameters. When setting the $\bar{b}$ in $^{13}\Delta_{simple}$ to the maximum likelihood estimates for calibrated model parameters (MLE) of 28‰ (Table 2), mean $^{13}\Delta_{obs}$ was underestimated during morning and late afternoon hours and generally overestimated during midday (BB2 and BB3, 1100 to 1400 h CET) by about 1.5‰. When using the more commonly reported $\bar{b}$ value of 27‰ for $^{13}\Delta_{simple}$ predictions, the midday overestimation decreased to about 0.5‰ for BB2 and BB3, while morning and afternoon predictions became worse for all branch bags (data not shown). Hourly means of the model predictive uncertainty (Fig. 2, shaded areas) also suggested greater predictive power for $^{13}\Delta_{comp}$ than for $^{13}\Delta_{simple}$, especially for BB1. Analysis of the mean diurnal variability further showed that both $^{13}\Delta_{simple}$ and $^{13}\Delta_{comp}$ predicted dawn observations slightly better than dusk observations by about 1‰ on average.

$^{13}\Delta_{simple}$ and $^{13}\Delta_{comp}$ model performances on day-to-day timescales

Day-to-day model performances were examined by comparing flux-weighted daily means of $^{13}\Delta_{obs}$ with those of $^{13}\Delta_{simple}$ and $^{13}\Delta_{comp}$ (Fig. 3). Flux-weighted daily means should provide a reasonable approximation of the daily integrated imprint of $^{13}\Delta$ on photosynthetic assimilates, and their assessment may thus benefit model choice for prospective model applications at daily resolutions. Between August and October, flux-weighted daily means of $^{13}\Delta_{obs}$ exhibited a steady increase that was less pronounced in the modelled values. Indeed, both models tended to overestimate $^{13}\Delta_{obs}$ in early August and underestimate $^{13}\Delta_{obs}$ in late September. This finding explained most of the deviation between predicted and observed values for $^{13}\Delta_{comp}$ (Table 2), despite the good model performance of $^{13}\Delta_{comp}$ over mean diurnal time courses (Fig. 2). Nonetheless, flux-weighted daily means of $^{13}\Delta_{comp}$ tracked observed day-to-day variations considerably better than flux-weighted daily means of $^{13}\Delta_{simple}$ (Fig. 3), despite little difference in RMSE values.

$^{13}\Delta_{simple}$ and $^{13}\Delta_{comp}$ parameter constraint and correlation

To be able to characterize the constraint on b in $^{13}\Delta_{comp}$, a relatively loose prior parameter uncertainty range had to be used (27–33‰) and MLE values for this parameter were subsequently found from 30.3 to 32.9‰ for the three branch bags (Table 2). These estimates of the fractionation factor b are slightly beyond the physiological range found by biochemical enzyme assays, but if the upper *a priori* bound for b was restricted to 30‰, b was never constrained and assigned to its upper bound. Similarly, for $^{13}\Delta_{simple}$, $\bar{b}$ was never constrained within the *a priori* limits and showed a clear tendency towards the upper bound with a resulting MLE of 28‰ for all three branch bags. In contrast, g_i in $^{13}\Delta_{comp}$ was well constrained with MLE values ranging between 0.15 and 0.18 mol m^{-2} s^{-1} depending on the branch bag data used (Table 2).

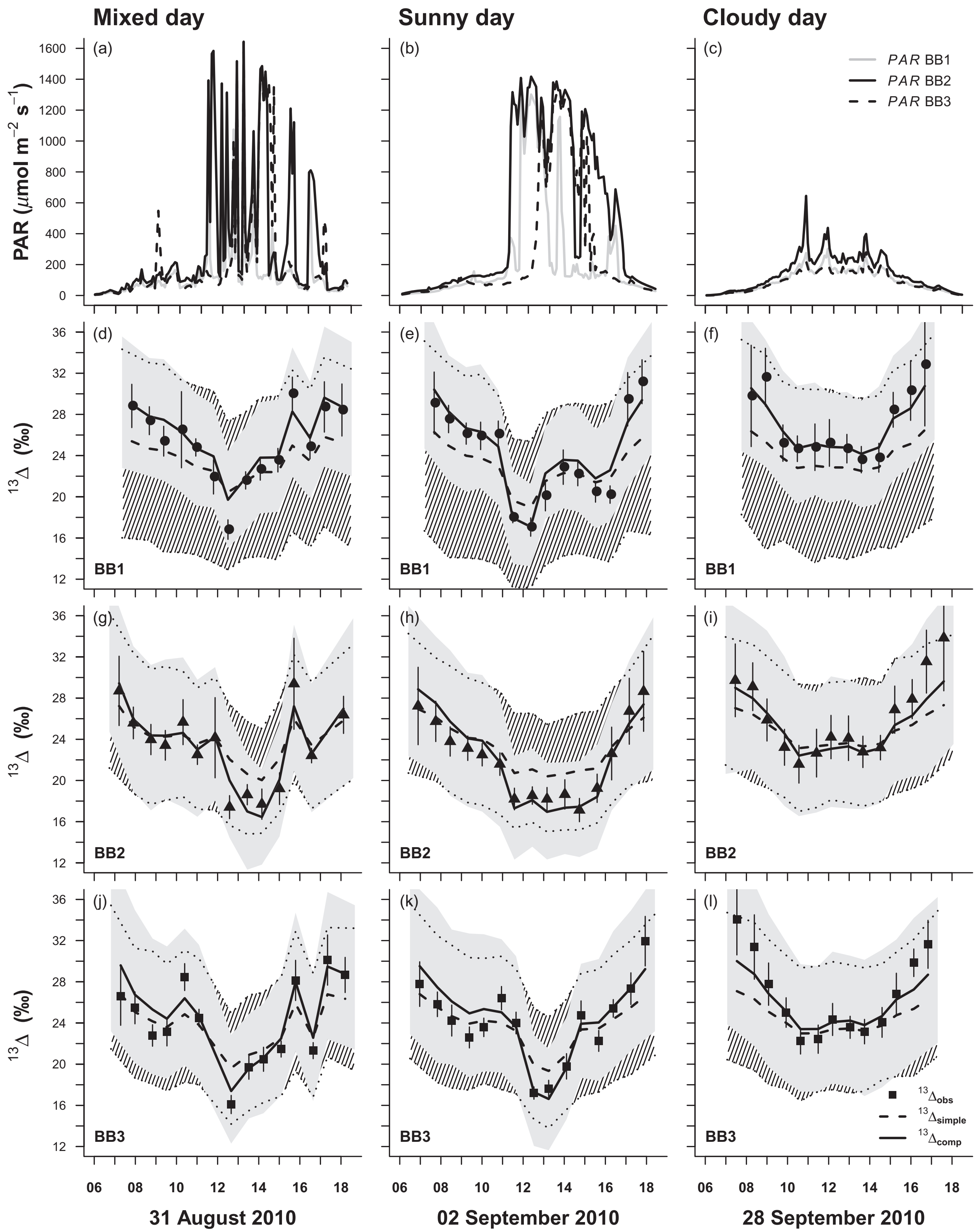

Figure 1. Photosynthetically active radiation (a to c) alongside observed and predicted $^{13}\Delta$ (d to l; showing data for three branch bags, BB1 to BB3) for three example days during the 2010 field campaign. Time axis unit is hour in CET. Symbol error bars represent ± one propagated SD for each $^{13}\Delta_{obs}$ measurement. The outer bounds of the model predictive uncertainty, characterized by the 2.5 and 97.5 percentiles ($Y_{2.5}$ and $Y_{97.5}$) are shown as hatched areas for $^{13}\Delta_{simple}$ and as shaded grey areas for $^{13}\Delta_{comp}$. $^{13}\Delta_{simple}$ and $^{13}\Delta_{comp}$ model predictions were calculated using MLE shown in Table 2.

Table 2. Summary of the $^{13}\Delta_{simple}$ and $^{13}\Delta_{comp}$ model calibration inputs and outputs as well as model performance measures for the $g_{s,mod}$ approach

			Prior parameter uncertainty ranges		Posterior parameter estimates		Posterior parameter uncertainty ranges		Model performance				
Model	PM	BB	Min	Max	MLE	Mean	P 2.5	P 97.5	Slope	Int.	r^2	max ln L	RMSE
Simple	$\bar{b}$	1	26	28	28.0	27.9	27.8	28.0	0.45	12.0	0.70	−1405	3.8
		2			28.0	27.8	27.5	28.0	0.47	12.8	0.71	−1400	2.9
		3			28.0	28.0	27.8	28.0	0.44	13.0	0.67	−1497	3.4
Comprehensive	g_i	1	0.10	0.50	0.15	0.16	0.13	0.19					
		2			0.18	0.19	0.16	0.22					
		3			0.18	0.18	0.15	0.23					
	b	1	27	33	32.9	32.8	32.3	32.9					
		2			30.3	30.4	29.7	31.2					
		3			31.1	31.4	30.6	32.1					
	f	1	8	12	8.0	8.6	8.0	10.1					
		2			8.1	8.4	8.0	9.5					
		3			8.0	8.5	8.0	9.7					
	e	1	−6	+6	−5.4	−4.2	−5.9	−0.1	0.81	5.0	0.71	−1275	2.6
		2			−5.7	−5.2	−6.0	−3.6	0.86	3.0	0.71	−1279	2.4
		3			−6.0	-5.5	−6.0	−4.0	0.76	5.9	0.67	−1400	2.7

Slopes and intercepts were calculated using standard major axis – regression (SMA, model2 – regession); r^2 was calculated with ordinary least square regression. Unit for g_i is mol m^{-2} s^{-1}; all other parameters expressed in ‰.
PM, estimated parameters; BB, branch bag; MLE, maximum likelihood estimate; P 2.5 and P 97.5, 2.5 and 97.5 percentiles for posterior parameter distributions; Int., intercept; max ln L, maximum of the natural logarithm of the negative likelihood; RMSE, root mean squared error.

The parameters f and e in $^{13}\Delta_{comp}$ could not be constrained, even with looser prior parameter uncertainty ranges. This is illustrated in Fig. 4 where the posterior distributions of g_i, b, f and e obtained from two different $^{13}\Delta_{comp}$ model calibration approaches are compared. If the prior parameter uncertainty ranges of f and e were set to previously reported values (8 to 12‰ for f and −6 to 6‰ for e), both parameters showed clear tendencies towards the specified lower limit (Fig. 4, left panels). If prior parameter uncertainty ranges were then considerably broadened, generally no constrained estimates were found for f and e. Only for BB2, a very weakly constrained estimate was found for e, yet well beyond the expected range (Fig. 4, right panels). We thus concluded that our measurement data contained only very little information about the fractionation factors f and e.

The g_i and b parameters also showed a dependency on f and e (Fig. 4). If f and e were free to resume values beyond their assumed physiological range (Fig. 4; right panel), the estimates of g_i and b decreased (Fig. 4, right panels). These dependencies between model parameters are quantified in Table 3, using parameter correlation coefficients obtained from the $^{13}\Delta_{comp}$ model calibration. The parameters g_i and b displayed a negative correlation that reflected their unidirectional effects on the term $b\frac{c_c}{c_a}$ in Eqn 3 (i.e. the higher g_i or b, the higher predictions of $^{13}\Delta_{comp}$). In contrast, we observed positive correlations between g_i and f and between b and e, indicating opposing effects of each pair on $^{13}\Delta_{comp}$ that explained the dependency of g_i and b on f and e. The relative importance of the different terms in Eqn 3 (see below) further explained why only large changes of f and e, well beyond their expected range, could improve the predictive power of $^{13}\Delta_{comp}$.

$^{13}\Delta_{comp}$ sensitivity analysis

To evaluate $^{13}\Delta_{comp}$ model performance on the basis of literature values, an additional sensitivity analysis was done, using variable values for b or g_i, and fixed values for f (11‰) and e (−6‰). Results for BB3 that exhibited an intermediate MLE for b (Table 2) are shown as an example (Fig. 5). When using a commonly accepted b value of 29‰ and a probable g_i value of 0.2 mol m^{-2} s^{-1} (Fig. 5, black dashed lines), the resulting RMSE (3.5‰) was only 0.8‰ greater than the RMSE shown in Table 2 and flux-weighted daily means were about 2‰ lower than with the fully calibrated $^{13}\Delta_{comp}$ model fits (Fig. 3), improving model performance at the beginning of August, but degrading it towards the end of the field campaign (Fig. 5, right panels).

The sensitivity analysis further showed how the interdependency between b and g_i influenced model behaviour and thus model calibration results (Fig. 5, left panels). An increase in g_i or b analogously improved $^{13}\Delta_{comp}$ model performance during midday. On the contrary, morning and afternoon predictions of $^{13}\Delta_{comp}$ were only improved with increasing b, but not with increasing g_i, after a certain threshold was reached. Hence, the RMSE decreased by only 0.1‰, if g_i was increased from 0.3 to 0.6 mol m^{-2} s^{-1}. This model behaviour explained our finding that the MLE of g_i did not increase when restricting the upper prior parameter uncertainty bound of b to 30‰ (data not shown), despite their large unidirectional effects on the term $b\frac{c_c}{c_a}$ of $^{13}\Delta_{comp}$.

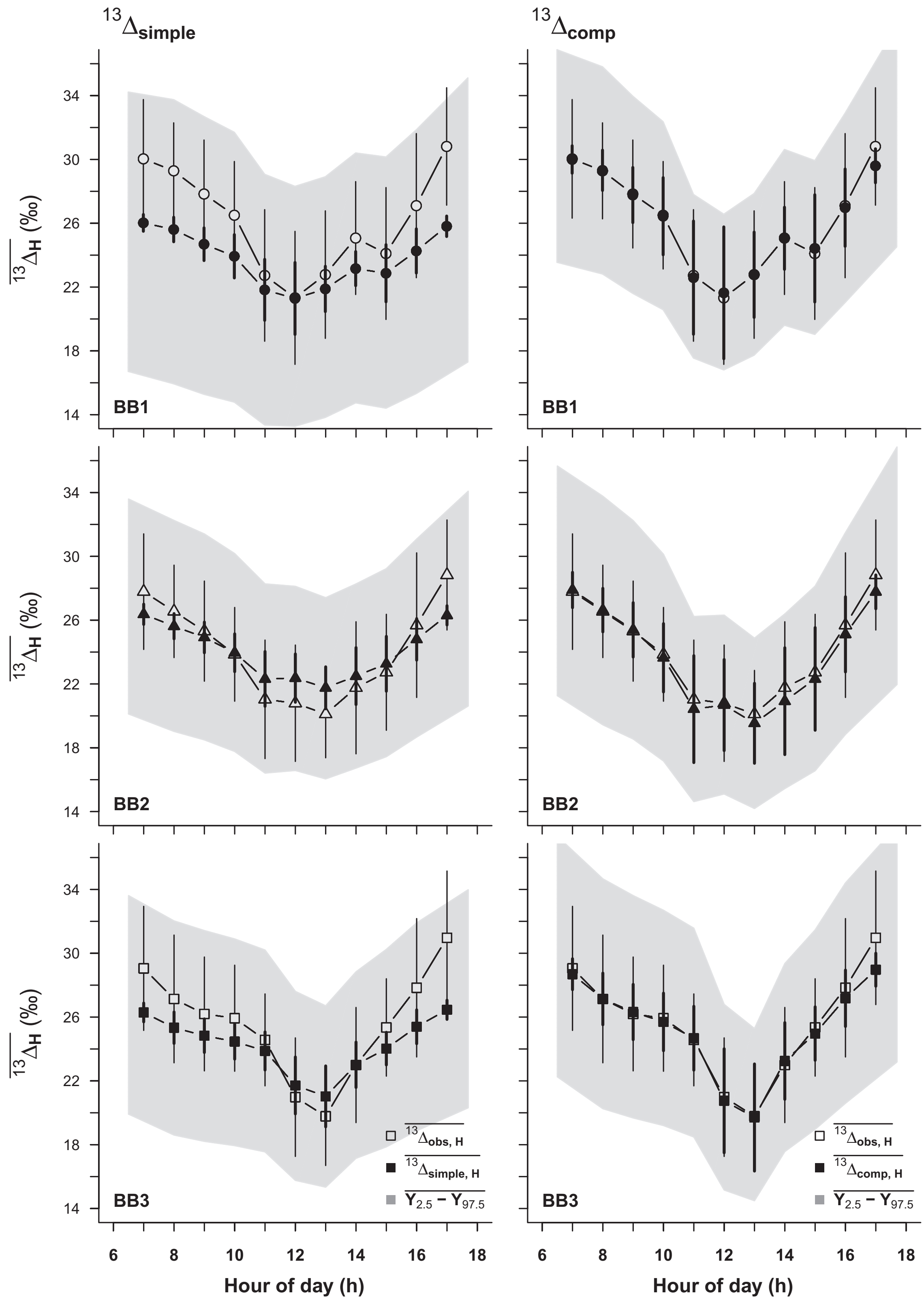

Figure 2. Mean diurnal variation of $^{13}\Delta_{obs}$ and corresponding model predictions for $^{13}\Delta_{simple}$ (left panel) and $^{13}\Delta_{comp}$ (right panel) for all days of the 2010 field campaign. Horizontal panels display data from three branch bags (BB1 to BB3). Error bars are ± one SD and represent day-to-day variability for $^{13}\Delta_{obs}$, $^{13}\Delta_{simple}$ and $^{13}\Delta_{comp}$. Shaded areas represent mean diurnals of the outer bounds of the model predictive uncertainty, characterized by the 2.5 and 97.5 percentiles ($Y_{2.5}$ and $Y_{97.5}$). $^{13}\Delta_{simple}$ and $^{13}\Delta_{comp}$ model predictions were calculated using MLE shown in Table 2.

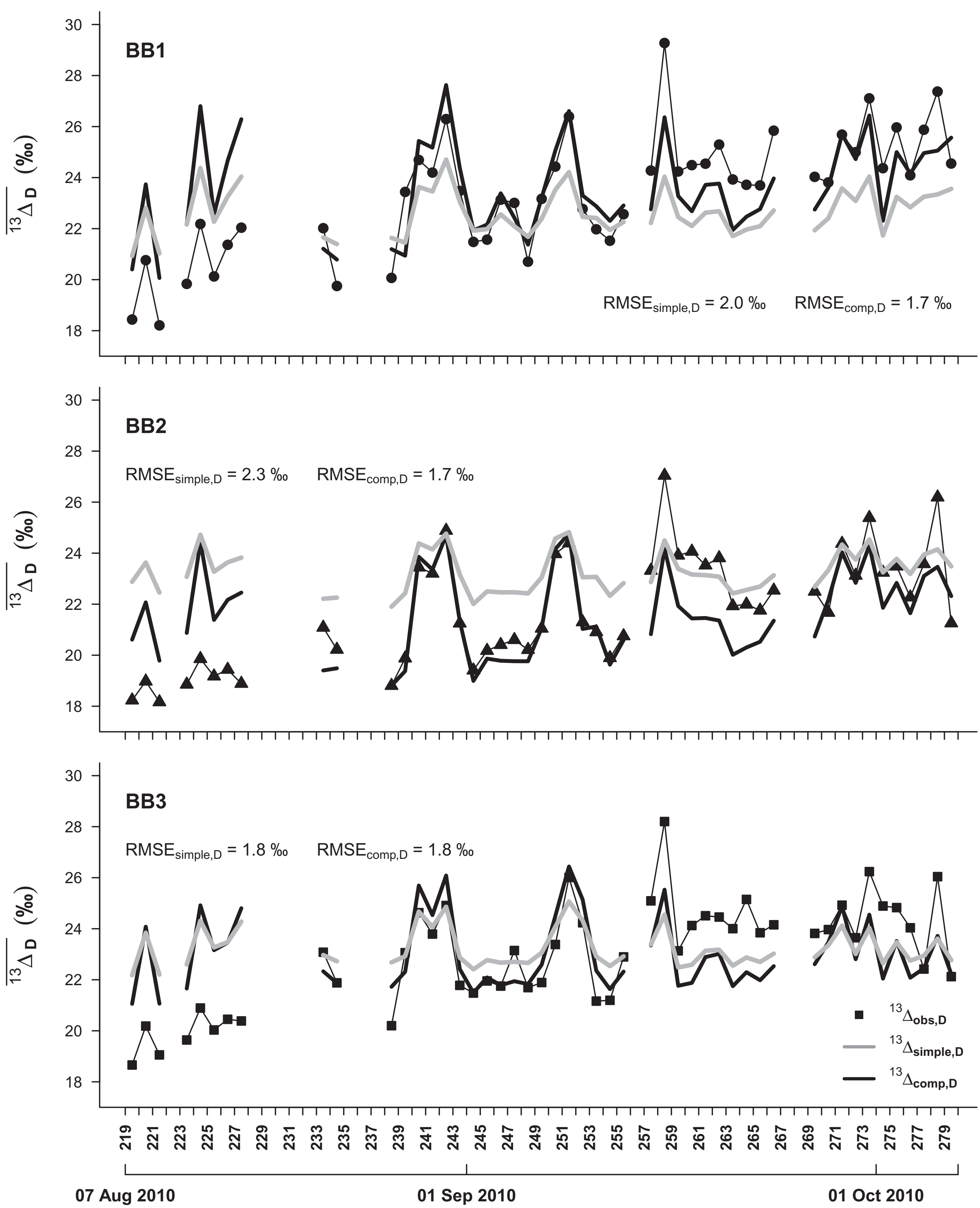

Figure 3. Flux-weighted daily arithmetic means of observed (symbols) and predicted (lines) $^{13}\Delta$ for the 2010 field campaign. Panels display data from the three branch bags (BB1 to BB3). Time axis unit is day of year. $^{13}\Delta_{simple}$ and $^{13}\Delta_{comp}$ model predictions were calculated using MLE shown in Table 2. RMSE$_D$ denote RMSE calculated based on flux-weighted daily arithmetic means (instead of single values).

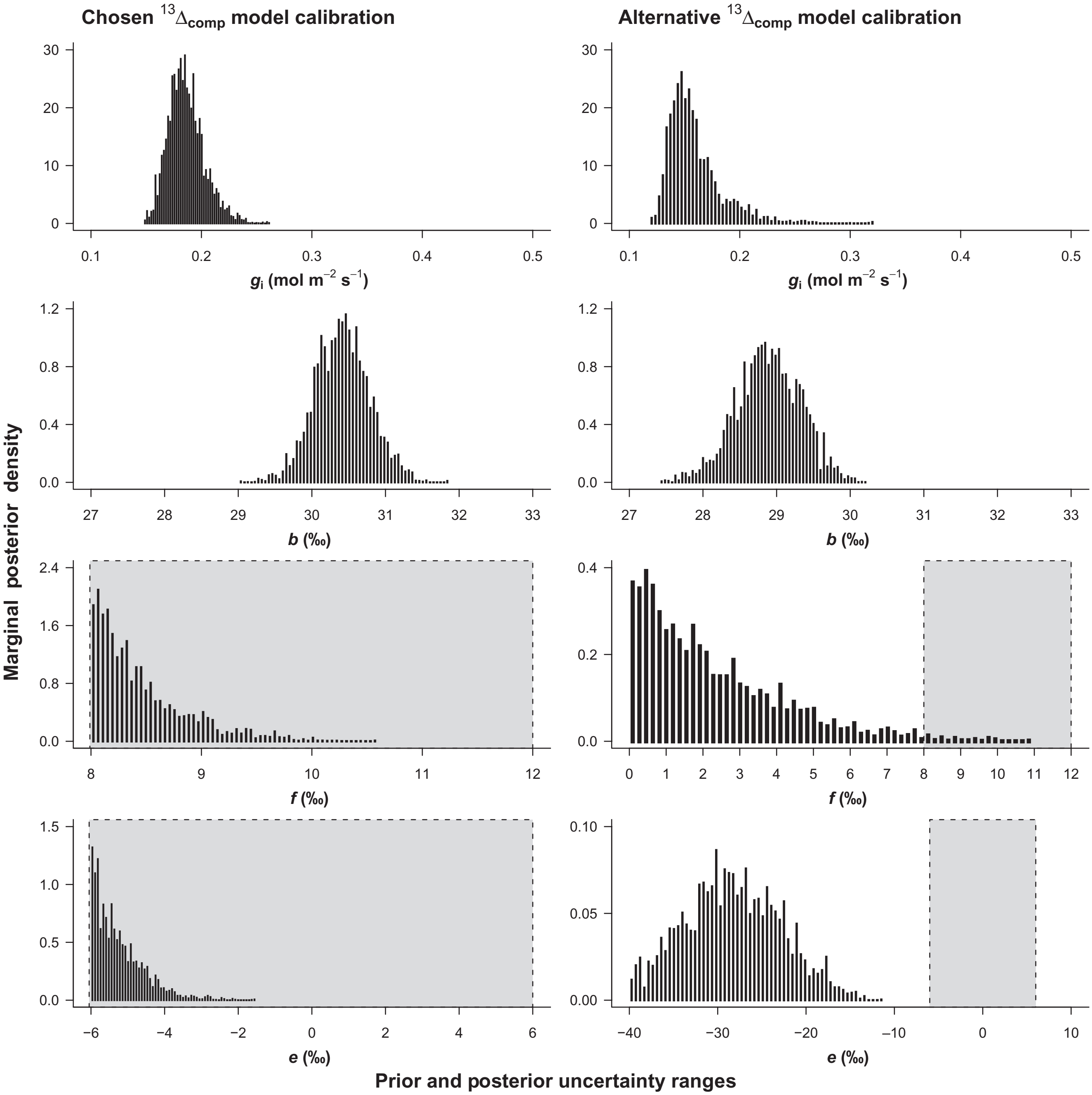

Figure 4. Marginal posterior densities of g_i, b, f and e, obtained from two different $^{13}\Delta_{comp}$ model calibration approaches. Left panels: model calibration approach shown in Fig. 1–3 with prior parameter uncertainty ranges for f and e set to values shown in Table 2. Right panels: alternative model calibration approach with broadened prior parameter uncertainty ranges for f and e. Shaded areas illustrate the different prior parameter uncertainty ranges used in these two approaches. All calculations were made with $g_{s,mod}$. Model output for BB2 was chosen as an example. Note: The dispersions on the x-axis of the marginal posterior densities shown in the left panels correspond to the posterior parameter uncertainty ranges reported in Table 2.

Impact of a temperature dependency for g_i

Implementing a temperature dependency of g_i (g_i^{25}) into $^{13}\Delta_{comp}$ led to a 0.6‰ decrease in b for BB2 and BB3, characterized by high midday temperatures, and no change in b for the more shaded BB1. While the constraint of f did not improve with g_i^{25}, its MLE increased to ≈ 10‰, except for BB1 (Table S5 in the SI). The correlation between b and g_i and b and e became even stronger with g_i^{25}. In contrast, the positive correlation between g_i and f completely disappeared for BB2 and BB3, and became negative for BB1 (Supporting Information Table S6). In addition, a new negative correlation between g_i and e appeared. Most importantly, a temperature–dependent g_i led to worse $^{13}\Delta_{comp}$ model performance and did

Table 3. Correlation matrix of the calibrated model parameters of $^{13}\Delta_{comp}$ for the $g_{s,mod}$ approach

R	g_i	*b*	*f*	*e*
g_i	BB1			
	BB2			
	BB3			
b	−0.39	BB1		
	−0.26	BB2		
	−0.18	BB3		
f	0.33	0.08	BB1	
	0.39	−0.03	BB2	
	0.34	0.14	BB3	
e	−0.06	0.14	−0.08	BB1
	−0.04	0.14	0.00	BB2
	−0.02	0.16	0.09	BB3

Prior parameter uncertainty ranges are identical to Table 2. Correlations are evaluated during repeated sampling from the posterior probability space and expressed by *R* values.

not improve the overall parameter constraint (Supporting Information Table S5).

$^{13}\Delta_{revised}$ model calibration

In order to explore whether there was a consistent pattern for the apparent fractionation factor e^* over the course of the diurnal cycle, we conducted three different model calibration approaches for $^{13}\Delta_{revised}$. Firstly, g_i, b, f and e were fixed to the MLE obtained for $^{13}\Delta_{comp}$ (Table 2) and distinct e^* estimates were sought for each hour of the day, choosing a prior parameter uncertainty range for e^* between −10 and 0‰. No consistent diurnal pattern of e^* was found and e^* was never constrained beyond its prior parameter uncertainty range for any hour of the day in any branch bag (not shown). Similar results were obtained when the parameters g_i, b, f and e were not fixed. Given the positive correlation between b and e, we further tested the effect of a lower b value on the estimation of e^*, using fixed parameter values of $g_i = 0.2$ mol m^{-2} s^{-1}, $b = 29$‰, $f = 11$‰ and $e = -6$‰, but this did not result in more constrained estimates of e^*.

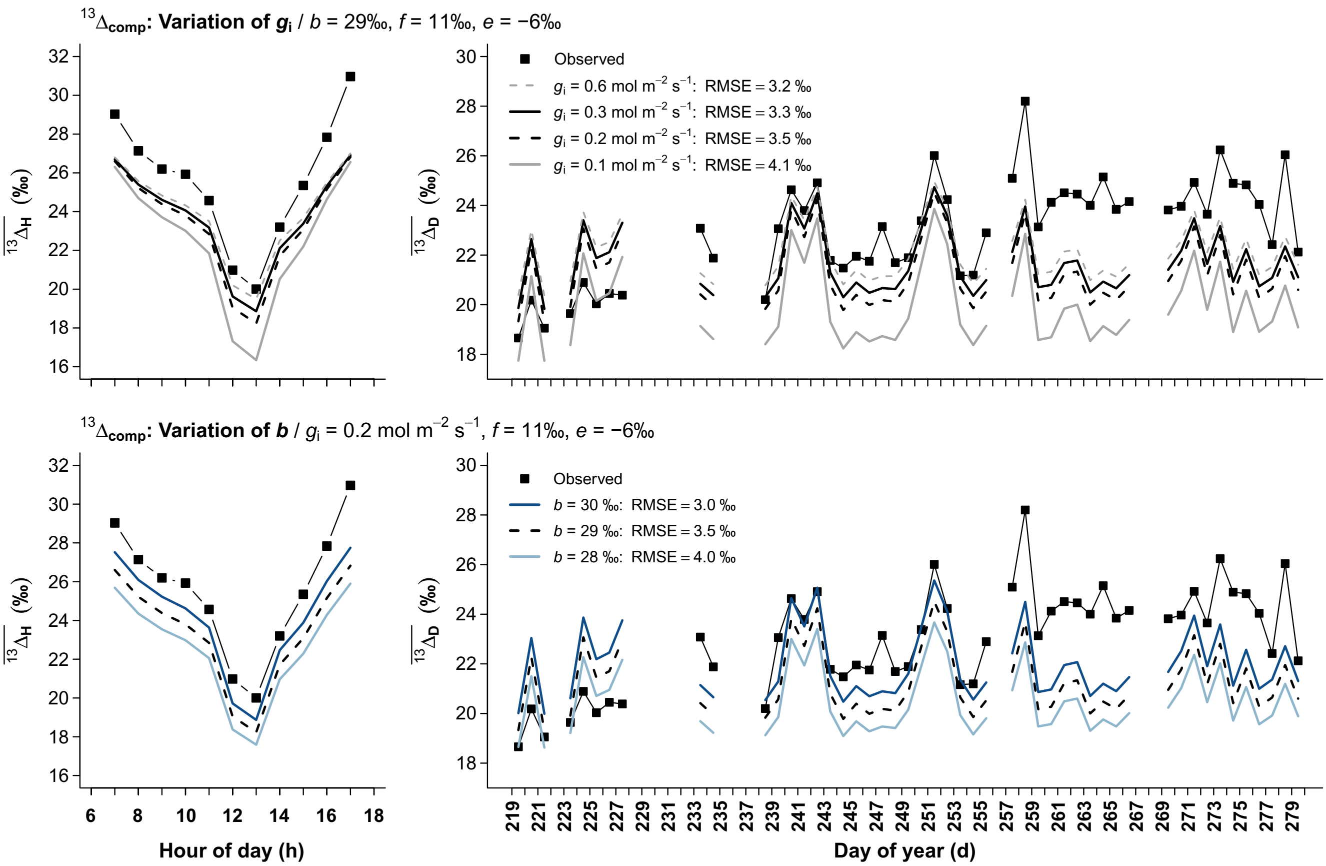

Figure 5. Sensitivity analysis for $^{13}\Delta_{comp}$. Either g_i (upper panel) or b (lower panel) is varied, while other parameters are fixed. Left panels show the mean diurnal variation of $^{13}\Delta_{obs}$ and different versions of $^{13}\Delta_{comp}$ for all days during the 2010 field campaign. Right panels show the corresponding flux-weighted daily arithmetic means of $^{13}\Delta_{obs}$ and $^{13}\Delta_{comp}$ for all days of the 2010 field campaign. All calculations were done with $g_{s,mod}$. Data from BB3 were chosen as example.

Contribution of single model terms to the mean diurnal cycle

The contribution of single model terms to the mean diurnal cycle of $^{13}\Delta_{simple}$ and $^{13}\Delta_{comp}$ is shown in Fig. 6 for BB3. Clearly, the better model performance of $^{13}\Delta_{comp}$ is largely driven by the c_c/c_a term that results in a more suitable description of the diurnal time course of $^{13}\Delta_{obs}$ compared with the c_i/c_a term in $^{13}\Delta_{simple}$ (Fig. 6). The diffusive terms in both models generally had a small effect (<1‰), and the photorespiratory term in $^{13}\Delta_{comp}$ played an important role in preventing midday overestimation of $^{13}\Delta_{obs}$ commonly observed with $^{13}\Delta_{simple}$. The contribution of the respiratory term was generally less than 0.2‰ for this dataset and the parameterization used.

Impact of g_s dataset on model calibration

Model calibrations of $^{13}\Delta_{simple}$ and $^{13}\Delta_{comp}$ mostly produced similar results if $g_{s,obs}$ was used instead of $g_{s,mod}$ for c_i calculations (see Supporting Information Tables S1 and S2). For $^{13}\Delta_{simple}$, $\bar{b}$ was never constrained and showed a clear tendency towards its upper bound (28‰). For $^{13}\Delta_{comp}$, b values were nearly equal to that obtained with the $g_{s,mod}$ approach, while the parameters f and e exhibited a similar behaviour to that described above, and no consistent and constrained patterns could be found for e^*. The main consequence of using $g_{s,obs}$, rather than $g_{s,mod}$ was that g_i was not constrained anymore for all three branch bags with MLE values close to the upper range of 0.50 mol m^{-2} s^{-1}. We also observed changes in the parameter correlation coefficients: the positive correlation between g_i and f disappeared and a new positive correlation between b and f was found.

Impact of ternary effects on $^{13}\Delta_{comp}$ model calibration

In general, the inclusion of ternary effects did not change $^{13}\Delta_{comp}$ parameter constraints and correlations for both the $g_{s,mod}$ and the $g_{s,obs}$ approaches, except for the case when b decreased on average by 0.9‰ and model performance became slightly worse (Supporting Information Table S3). Parameter correlations did not change for the most part when $g_{s,obs}$ was used. With $g_{s,mod}$, the correlation between b and g_i became stronger (more negative), while that between g_i and f became slightly weaker (Supporting Information Table S4). In order to explore the influence of ternary corrections during changing temperature and humidity regimes, model residuals of $^{13}\Delta_{comp}$ and $^{13}\Delta_{comp,TERN}$ were plotted against the concurrent leaf-to-air vapour pressure deficit. The overall distribution of model residuals was, however, not different between $^{13}\Delta_{comp}$ and $^{13}\Delta_{comp,TERN}$ (Supporting Information Fig. S1).

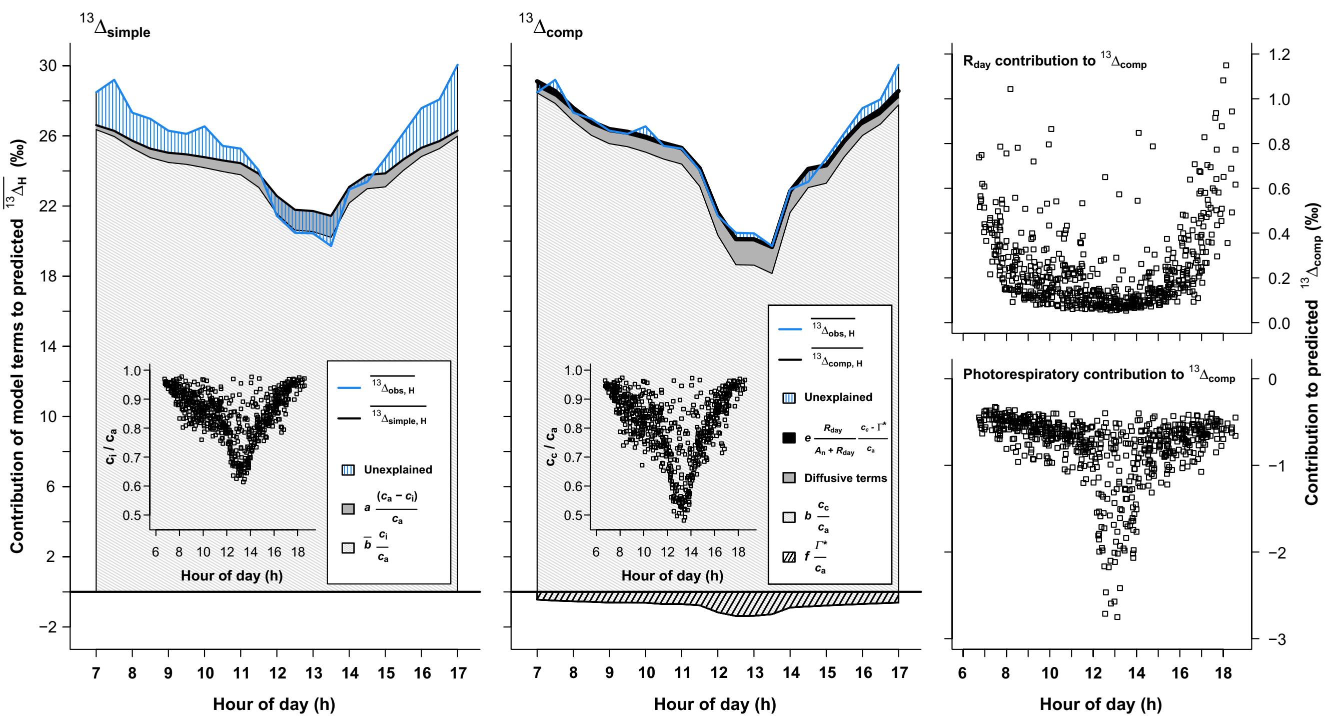

Figure 6. Contribution of single model terms of $^{13}\Delta_{simple}$ (Eqn 5) and $^{13}\Delta_{comp}$ (Eqn 3) to the total predicted $^{13}\Delta$. Data from BB3 were chosen as example. Left and middle panels: mean diurnal contributions to $^{13}\Delta_{simple}$ and $^{13}\Delta_{comp}$. Right panels: diurnal courses of the $^{13}\Delta_{comp}$ model terms $e\dfrac{R_{day}}{A_n + R_{day}}\dfrac{c_c - \Gamma^*}{c_a}$ (upper panel) and $f\dfrac{\Gamma^*}{c_a}$ (lower panel) for all predicted data points. Presented half-hourly means were calculated using MLE shown in Table 2.

DISCUSSION

$^{13}\Delta_{comp}$ model behaviour and parameter interdependencies

The Bayesian approach used here for calibrating models of $^{13}\Delta$ could not provide well-constrained estimates for all model parameters. However, the method emphasized the strong drivers of the models (i.e. the model term $b\frac{c_c}{c_a}$ and thus b and g_i), and other drivers with only a slight impact under particular circumstances (i.e. the respiratory and photorespiratory model terms and thus f, e or e^*). The respiratory term $e\frac{R_{day}}{A_n + R_{day}}\frac{c_c - \Gamma^*}{c_a}$ only played a significant role at times with low net CO_2 assimilation (A_n), commonly occurring in the early morning and in the late afternoon (Fig. 6), while the photorespiratory term $f\frac{\Gamma^*}{c_a}$ mainly decreased $^{13}\Delta_{comp}$ at midday (Fig. 6) when high temperatures significantly increased Γ^* (the term $f\frac{\Gamma^*}{c_a}$ is preceded by a minus sign in Eqn 3).

The method and the 60-day-long dataset were ideal for studying and quantifying parameter interdependencies. A strong negative correlation between g_i and b originated from their unidirectional effects on the dominant term $b\frac{c_c}{c_a}$. Positive correlations between g_i and f and between b and e were also found, mainly because $^{13}\Delta_{comp}$ tended to underestimate $^{13}\Delta_{obs}$ (Figs. 2 & 5), so that the model calibration aimed to increase $^{13}\Delta_{comp}$. At midday, when $^{13}\Delta_{comp}$ was also most sensitive to changes in g_i (Fig. 5) and in the photorespiratory term (see above), an increase in $^{13}\Delta_{comp}$ could only be achieved by either increasing g_i (Fig. 5) or decreasing f, leading to the observed positive correlation between the two parameters (Table 3). In early morning and late afternoon, when the respiratory term was most important, the underestimation by $^{13}\Delta_{comp}$ could be overcome best by either increasing b or decreasing e (Fig. 4), leading also to a positive correlation between these two parameters (Table 3). This understanding of the $^{13}\Delta_{comp}$ model behaviour over diurnal cycles could also explain the observed effects of a temperature-dependent g_i on $^{13}\Delta_{comp}$. At midday, the temperature-dependent g_i was higher than the constant g_i, and led to higher $^{13}\Delta_{comp}$ even with a lower b and a higher f, while during early morning and late afternoon hours, the temperature-dependent g_i was lower than a constant g_i, and resulted in a stronger underestimation of $^{13}\Delta_{obs}$. The model calibration tried to overcome this underestimation with a decrease in e. The correlation analysis revealed a stronger interaction between f and b and a new correlation between g_i and e that was driven by a new early morning and late afternoon interaction between these parameters during the $^{13}\Delta_{comp}$ model calibration. Interestingly, both b and f estimates moved slightly closer to their physiological range when a temperature-dependent g_i was used, supporting the idea of a variable g_i (see below).

Model calibration for $^{13}\Delta_{comp,TERN}$ resulted in a lower b compared with when ternary effects were neglected (Supporting Information Table S3). This decrease in b was driven by a similar mechanism as the one evoked for the model calibration with temperature-dependent g_i because ternary effect corrections (like the temperature-dependent g_i) mainly led to a stronger decrease of c_c/c_a at midday, that is, when the evaporative demand (the leaf-to-air vapour mole fraction differences) was large. The overall effect was, however, so small that model residuals for $^{13}\Delta_{comp}$ and $^{13}\Delta_{comp,TERN}$ did not show any clear differences when plotted against the leaf-to-air vapour pressure deficit (Supporting Information Fig. S1).

Previous studies have also reported interdependencies between the $^{13}\Delta_{comp}$ model parameters. Using a regression approach that treated g_i, b and f as unknowns, Lanigan *et al.* (2008) demonstrated the dependency of f estimates on assumed values of b and g_i in a laboratory study on *Senecio* species. Recently, Evans & von Caemmerer (2013) demonstrated a positive linear dependency between b and f estimates. Over a 25 K temperature range, they also showed that a decrease of the $b\frac{c_c}{c_a}$ term (*via* a decrease in g_i), and an increase of the $f\frac{\Gamma^*}{c_a}$ term (via an increase in Γ^*) roughly cancelled out any temperature dependency of the observed $^{13}\Delta$. Using a sensitivity analysis, Wingate *et al.* (2007) also illustrated interdependencies between b, e and e^* for $^{13}\Delta_{comp}$ and $^{13}\Delta_{revised}$ predictions over the diurnal cycle in a field study on *P. sitchensis*. The current study nicely complements these results by treating all the parameters equally and using a 60-day-long dataset. However, this general pattern of interdependency between parameters indicates that controlled laboratory experiments simultaneously combining additional approaches, such as fluorescence and ^{13}C labelling will be necessary to constrain better certain parameters and to reveal the response of the photosynthetic and respiratory machinery to environmental drivers.

Consequences for g_i estimates

Manipulations of Eqns 3 and 5 are commonly used to derive estimates of g_i (Evans *et al.* 1986; Lloyd *et al.* 1992; Pons *et al.* 2009). The g_i estimation method relies on a number of assumptions, including full predictability of $^{13}\Delta_{obs}$ by $^{13}\Delta_{comp}$, and thus displays similar sensitivities as $^{13}\Delta_{comp}$ model calibrations. For example, in a laboratory study on *Arabidopis thaliana* (L.), *Nicotiana tabacum* (L.) and *Triticum aestivum* (L.), Tazoe *et al.* (2011) showed a large effect of b on the calculated g_i values, but small effects of f and e. However, this small sensitivity to respiratory terms is likely to depend on the environmental conditions or the plant species. For example, using $^{13}\Delta_{obs}$ data from a field study, Bickford *et al.* (2009) found that g_i estimates for *Juniperus monosperma* (Engelm.) were strongly dependent on the values used for e and f. Likewise, Douthe *et al.* (2011), working with *Eucalyptus* species under laboratory conditions, found that absolute g_i estimates were up to 50% larger when respiratory and photorespiratory terms of $^{13}\Delta_{comp}$ were considered for g_i calculations. Our study also indicates that g_i is strongly and negatively correlated with b and positively correlated with f but also e (assuming g_i depends on temperature). It also provides a way forward for estimating g_i and its uncertainty, without having to fix the other parameters.

Constant versus variable g_i

Evidence is increasing that g_i is most likely variable (Flexas *et al.* 2012). So far, studies investigating seasonal changes of g_i have not found a direct seasonal effect (e.g. Montpied *et al.* 2009; Ubierna & Marshall 2011) and evidence for a g_i decline with leaf age is also conflicting (e.g. Loreto *et al.* 1994; Ethier *et al.* 2006; Whitehead *et al.* 2011). The sensitivity analysis shown in Fig. 5 illustrates that the implementation of a seasonal decline of g_i would have deteriorated overall $^{13}\Delta_{comp}$ model performance. Recent studies have further indicated the existence of short-term responses of g_i to environmental variables. Increasing irradiance (Flexas *et al.* 2008 and references therein; Douthe *et al.* 2011) tends to increase g_i, while an increasing CO_2 mole fraction commonly results in a g_i decrease (Hassiotou *et al.* 2009 and references therein; Douthe *et al.* 2011; Tazoe *et al.* 2011; Flexas *et al.* 2012). Evans & von Caemmerer (2013) recently reinforced the idea that temperature is a major driver of g_i (Bernacchi *et al.* 2002; Warren & Dreyer 2006; Warren 2008). Our results are more contrasted: the temperature dependence of g_i led b and f to come closer to their physiological ranges but on the other hand the model performance became slightly worse than when g_i was constant. However, stronger diurnal variations in say e^* may have sufficed to improve model performance (Wingate *et al.* 2007; Tcherkez *et al.* 2011b), even with a variable g_i.

Differences between the two g_s datasets

The Ball–Berry approach prescribed each branch a defined stomatal response to observed A_n, h_s and c_s (Eqn 2), known drivers of stomatal opening (Collatz *et al.* 1991), but other regulatory mechanisms of stomatal opening, such as root-derived hormonal signals (Damour *et al.* 2010) or seasonal acclimation (Kutsch *et al.* 2001), would not have been accounted for. However, a direct comparison between instantaneous $^{13}\Delta_{comp}$ values calculated with either $g_{s,mod}$ or with $g_{s,obs}$ (data shown in the Supporting Information) indicated that the magnitude of $^{13}\Delta_{comp}$ values was comparable for both approaches over the entire field campaign. Using observed g_s mostly altered the value and the constraint of g_i as well as its correlation with f. In general, we cannot rule out that g_s measurements were without error, as field measurements of g_s are notoriously difficult to make. However, the observed loss of correlation between g_i and f, when using $g_{s,obs}$ instead of $g_{s,mod}$ values, was most likely caused by the quality filtering of $g_{s,obs}$ data that led to an underrepresentation of midday values in the respective model calibrations (see Materials and methods). This underrepresentation probably influenced parameter correlation, given the high sensitivity of $^{13}\Delta_{comp}$ to g_i during midday (Fig. 5).

Parametrization and constraint of e and e^*

The small contribution of the R_{day} term in Eqn 3 to total predicted $^{13}\Delta_{comp}$ (Fig. 6) mainly originated from the small magnitude of R_{day}. During night-time, measured branch respiration rates were on average 0.1 to 0.2 μmol m^{-2} s^{-1} at leaf temperatures between 10 to 15 °C. These rates were consistent with the range reported by Seibt *et al.* (2007) for leafy beech branches in the lower canopy. It showed a pronounced dependency on leaf temperature and our fitted Q_{10} values matched those previously reported for beech (Atkin *et al.* 2005), thus providing confidence in the measurements. Under light, and thus during daytime, mitochondrial respiration is believed to be down-regulated (Atkin *et al.* 2005; Lee *et al.* 2010), and mechanistic models describing this are only just beginning to emerge (Buckley & Adams 2011). Given the lack of quantitative approaches to model R_{day}, we simply assumed a 50% reduction (Tcherkez *et al.* 2005) of R_{day} compared with the leaf temperature-dependent nocturnal branch respiration. At a leaf temperature of 25 °C, R_{day} estimates ranged between 0.1 and 0.2 μmol m^{-2} s^{-1} and matched estimates obtained from photosynthetic light response curves (Marshall & Biscoe 1980), fitted to each branch bag. Additional tests without any light inhibition of R_{day} did not show an increasing constraint of e or substantial change for any other calibrated parameter, including e^* and even when mean hourly e^* values were the only parameters to be estimated. This finding indicated the absence of a consistent diurnal pattern for an isotopic disequilibrium between substrates fuelling R_{day} and current assimilates. Day-to-day changes in the contribution of older and current carbon to the R_{day} substrate pool could have counteracted the constraint of e^*. Such changes could have originated from changes in cumulative daily assimilation or temperature that are likely to influence substrate supply and use; however, it was beyond the scope of the current study to explore this possibility.

Model choice

Our results support the view that more detailed versions of the $^{13}\Delta$ model are better suited than $^{13}\Delta_{simple}$ for predicting instantaneous $^{13}\Delta_{obs}$ in the field (Wingate *et al.* 2007). Roughly equal model performances of $^{13}\Delta_{simple}$ and $^{13}\Delta_{comp}$, as reported by Bickford *et al.* (2009, 2010), were found for individual days (see Supporting Information), but were not the rule (Fig. 2). Our model exercise showed that the better performance of $^{13}\Delta_{comp}$ (compared with $^{13}\Delta_{simple}$) over diurnal time courses originated to a large extent in the assumption of a finite g_i and the inclusion of the photorespiratory term (Fig. 6), and consequently, encourages the ongoing use of these terms in models predicting $^{13}\Delta$ variations at an hourly timescale (e.g. Ogée *et al.* 2003; Suits 2005; Cai *et al.* 2008; Zobitz *et al.* 2008; Ogée *et al.* 2009). At the daily timescale, $^{13}\Delta_{comp}$ also performed better than $^{13}\Delta_{simple}$ to predict flux-weighted daily means of $^{13}\Delta_{obs}$, but only for two of the three branches (Fig. 3). Whether this better performance of $^{13}\Delta_{comp}$ compared with $^{13}\Delta_{simple}$ is maintained at seasonal or inter-annual timescales remains unknown. Thus, general recommendations for the use of $^{13}\Delta_{comp}$ for applications at such long timescales cannot be made.

ACKNOWLEDGMENTS

We thank EMPA for the permission to use the Lägeren NABEL station and for provision of meteorological site data to the Grassland Sciences group, ETH Zurich. For enduring help in the field, we thank all involved fellow members of the Grassland Sciences group, ETH apprentices and student assistants, especially Laura Spring and Daniela Cervenka. We are in particular grateful to Matti Barthel for his overall support and many fruitful discussions. We further thank all ETH workshops that contributed to the branch bag assembly and the Lägeren forester, Philipp Vock. This study was financed by a Marie Curie Excellence Grant from the European Commission to A.K. (Project No.: MEXT-CT-2006–042268) and benefited from a SIBAE STSM Grant to L.G. (COST-STSM-ECOST-STSM-ES0806–280211-005035). The INRA department EFPA is also acknowledged for funding the sabbatical of J.O. in Cambridge and salary for L.G. that resulted in the finalization of this manuscript.

REFERENCES

Atkin O.K., Bruhn D., Hurry V.M. & Tjoelker M.G. (2005) The hot and the cold: unravelling the variable response of plant respiration to temperature. *Functional Plant Biology* **32,** 87–105.

Baldocchi D.D. & Bowling D.R. (2003) Modelling the discrimination of $^{13}CO_2$ above and within a temperate broad-leaved forest canopy on hourly to seasonal time scales. *Plant, Cell and Environment* **26,** 231–244.

Ballantyne A.P., Miller J.B. & Tans P.P. (2010) Apparent seasonal cycle in isotopic discrimination of carbon in the atmosphere and biosphere due to vapor pressure deficit. *Global Biogeochemical Cycles* **24,** 3018–3034.

Ballantyne A.P., Miller J.B., Baker I.T., Tans P.P. & White J.W.C. (2011) Novel applications of carbon isotopes in atmospheric CO_2: what can atmospheric measurements teach us about processes in the biosphere? *Biogeosciences* **8,** 3093–3106.

BAFU (2011) *NABEL – Luftbelastung 2010. Messresultate des Nationalen Beobachtungsnetzes für Luftfremdstoffe (NABEL). Umwelt-Zustand Nr. 1118*. Bundesamt für Umwelt (BAFU), Bern, Switzerland.

Bernacchi C.J., Singsaas E.L., Pimentel C., Portis A.R. & Long S.P. (2001) Improved temperature response functions for models of Rubisco-limited photosynthesis. *Plant, Cell and Environment* **24,** 253–259.

Bernacchi C.J., Portis A.R., Nakano H., von Caemmerer S. & Long S.P. (2002) Temperature response of mesophyll conductance. Implications for the determination of Rubisco enzyme kinetics and for limitations to photosynthesis in vivo. *Plant Physiology* **130,** 1992–1998.

Betson N.R., Johannisson C., Löfvenius M.O., Grip H., Granström A. & Högberg P. (2007) Variation in the $\delta^{13}C$ of foliage of *Pinus sylvestris* L. in relation to climate and additions of nitrogen: analysis of a 32-year chronology. *Global Change Biology* **13,** 2317–2328.

Bickford C.P., McDowell N.G., Erhardt E.B. & Hanson D.T. (2009) High-frequency field measurements of diurnal carbon isotope discrimination and internal conductance in a semi-arid species, *Juniperus monosperma*. *Plant, Cell and Environment* **32,** 796–810.

Bickford C.P., Hanson D.T. & McDowell N.G. (2010) Influence of diurnal variation in mesophyll conductance on modelled ^{13}C discrimination: results from a field study. *Journal of Experimental Botany* **61,** 3223–3233.

Bowling D.R., Tans P.P. & Monson R.K. (2001) Partitioning net ecosystem carbon exchange with isotopic fluxes of CO_2. *Global Change Biology* **7,** 127–145.

Buck A.L. (1981) New equations for computing vapor-pressure and enhancement factor. *Journal of Applied Meteorology* **20,** 1527–1532.

Buckley T.N. & Adams M.A. (2011) An analytical model of non-photorespiratory CO_2 release in the light and dark in leaves of C_3 species based on stoichiometric flux balance. *Plant, Cell & Environment* **34,** 89–112.

von Caemmerer S. & Farquhar G.D. (1981) Some relationships between the biochemistry of photosynthesis and the gas exchange of leaves. *Planta* **153,** 376–387.

Cai T., Flanagan L.B., Jassal R.S. & Black T.A. (2008) Modelling environmental controls on ecosystem photosynthesis and the carbon isotope composition of ecosystem-respired CO_2 in a coastal Douglas-fir forest. *Plant, Cell and Environment* **31,** 435–453.

Chen B. & Chen J.M. (2007) Diurnal, seasonal and interannual variability of carbon isotope discrimination at the canopy level in response to environmental factors in a boreal forest ecosystem. *Plant, Cell & Environment* **30,** 1223–1239.

Collatz G.J., Ball J.T., Grivet C. & Berry J.A. (1991) Physiological and environmental regulation of stomatal conductance, photosynthesis and transpiration – a model that includes a laminar boundary layer. *Agricultural and Forest Meteorology* **54,** 107–136.

Damour G., Simonneau T., Cochard H. & Urban L. (2010) An overview of models of stomatal conductance at the leaf level. *Plant, Cell & Environment* **33,** 1419–1438.

Douthe C., Dreyer E., Epron D. & Warren C.R. (2011) Mesophyll conductance to CO_2, assessed from online TDL-AS records of $^{13}CO_2$ discrimination, displays small but significant short-term responses to CO_2 and irradiance in *Eucalyptus* seedlings. *Journal of Experimental Botany* **62,** 5335–5346.

Ekblad A., Boström B., Holm A. & Comstedt D. (2005) Forest soil respiration rate and $\delta^{13}C$ is regulated by recent above ground weather conditions. *Oecologia* **143,** 136–142.

Ethier G.J., Livingston N.J., Harrison D.L., Black T.A. & Moran J.A. (2006) Low stomatal and internal conductance to CO_2 versus Rubisco deactivation as determinants of the photosynthetic decline of ageing evergreen leaves. *Plant, Cell and Environment* **29,** 2168–2184.

Eugster W., Zeyer K., Zeeman M., Michna P., Zingg A., Buchmann N. & Emmenegger L. (2007) Methodical study of nitrous oxide eddy covariance measurements using quantum cascade laser spectrometery over a Swiss forest. *Biogeosciences* **4,** 927–939.

Evans J.R. & von Caemmerer S. (2013) Temperature response of carbon isotope discrimination and mesophyll conductance in tobacco. *Plant, Cell and Environment* **36,** 745–756.

Evans J.R., Sharkey T.D., Berry J.A. & Farquhar G.D. (1986) Carbon isotope discrimination measured concurrently with gas exchange to investigate CO_2 diffusion in leaves of higher plants. *Australian Journal of Plant Physiology* **13,** 281–292.

Farquhar G.D. & Cernusak L.A. (2012) Ternary effects on the gas exchange of isotopologues of carbon dioxide. *Plant, Cell & Environment* **35,** 1221–1231.

Farquhar G.D. & Richards R.A. (1984) Isotopic composition of plant carbon correlates with water-use efficiency of wheat genotypes. *Australian Journal of Plant Physiology* **11,** 539–552.

Farquhar G.D., O'Leary M.H. & Berry J.A. (1982) On the relationship between carbon isotope discrimination and the intercellular carbon dioxide concentration in leaves. *Australian Journal of Plant Physiology* **9,** 121–137.

Farquhar G.D., Ehleringer J.R. & Hubick K.T. (1989) Carbon isotope discrimination and photosynthesis. *Annual Review of Plant Physiology and Plant Molecular Biology* **40,** 503–537.

Flexas J., Ribas-Carbo M., Diaz-Espejo A., Galmes J. & Medrano H. (2008) Mesophyll conductance to CO_2: current knowledge and future prospects. *Plant, Cell and Environment* **31,** 602–621.

Flexas J., Barbour M.M., Brendel O., Cabrera H.M., Carriquí M., Díaz-Espejo A., . . . Warren C.R. (2012) Mesophyll diffusion conductance to CO2: an unappreciated central player in photosynthesis. *Plant Science* **193–194,** 70–84.

Ghashghaie J., Badeck F.-W., Lanigan G., Nogues S., Tcherkez G., Deleens E., . . . Griffiths H. (2003) Carbon isotope fractionation during dark respiration and photorespiration in C_3 plants. *Phytochemistry Reviews* **2,** 145–161.

Guy R.D., Fogel M.L. & Berry J.A. (1993) Photosynthetic fractionation of the stable isotopes of oxygen and carbon. *Plant Physiology* **101,** 37–47.

Harwood K.G., Gillon J.S., Griffiths H. & Broadmeadow M.S.J. (1998) Diurnal variation of $\Delta^{13}CO_2$, $\Delta C^{18}O^{16}O$ and evaporative site enrichment of $\delta H_2{}^{18}O$ in *Piper aduncum* under field conditions in Trinidad. *Plant, Cell and Environment* **21,** 269–283.

Hassiotou F., Ludwig M., Renton M., Veneklaas E.J. & Evans J.R. (2009) Influence of leaf dry mass per area, CO_2, and irradiance on mesophyll conductance in sclerophylls. *Journal of Experimental Botany* **60,** 2303–2314.

Igamberdiev A.U., Mikkelsen T.N., Ambus P., Bauwe H., Lea P.J. & Gardestrom P. (2004) Photorespiration contributes to stomatal regulation and carbon isotope fractionation: a study with barley, potato and *Arabidopsis* plants deficient in glycine decarboxylase. *Photosynthesis Research* **81,** 139–152.

Jarman P.D. (1974) Diffusion of carbon dioxide and water vapor through stomata. *Journal of Experimental Botany* **25,** 927–936.

Jones H.G. (1992) *Plants and Microclimate: A Quantitative Approach to Environmental Plant Physiology*. Cambridge University Press, Cambridge.

Kaiser J. (2008) Reformulated ^{17}O correction of mass spectrometric stable isotope measurements in carbon dioxide and a critical appraisal of historic 'absolute' carbon and oxygen isotope ratios. *Geochimica et Cosmochimica Acta* **72,** 1312–1334.

Keitel C., Adams M.A., Holst T., Matzarakis A., Mayer H., Rennenberg H. & Gessler A. (2003) Carbon and oxygen isotope composition of organic compounds in the phloem sap provides a short-term measure for stomatal conductance of European beech (*Fagus sylvatica* L.). *Plant, Cell and Environment* **26,** 1157–1168.

Knohl A. & Buchmann N. (2005) Partitioning the net CO_2 flux of a deciduous forest into respiration and assimilation using stable carbon isotopes. *Global Biogeochemical Cycles* **19,** 4008–4022.

Knohl A., Werner R.A., Brand W.A. & Buchmann N. (2005) Short-term variations in $\delta^{13}C$ of ecosystem respiration reveals link between assimilation and respiration in a deciduous forest. *Oecologia* **142,** 70–82.

Kutsch W.L., Herbst M., Vanselow R., Hummelshoj P., Jensen N.O. & Kappen L. (2001) Stomatal acclimation influences water and carbon fluxes of a beech canopy in northern Germany. *Basic and Applied Ecology* **2,** 265–281.

Lanigan G.J., Betson N., Griffiths H. & Seibt U. (2008) Carbon isotope fractionation during photorespiration and carboxylation in *Senecio*. *Plant Physiology* **148,** 2013–2020.

Lee C.P., Eubel H. & Millar A.H. (2010) Diurnal changes in mitochondrial function reveal daily optimization of light and dark respiratory metabolism in *Arabidopsis*. *Molecular & Cellular Proteomics* **9,** 2125–2139.

Lloyd J., Syvertsen J.P., Kriedemann P.E. & Farquhar G.D. (1992) Low conductances for CO_2 diffusion from stomata to the sites of carboxylation in leaves of woody species. *Plant, Cell and Environment* **15,** 873–899.

Loreto F., Dimarco G., Tricoli D. & Sharkey T.D. (1994) Measurements of mesophyll conductance, photosynthetic electron-transport and alternative electron sinks of field-grown wheat leaves. *Photosynthesis Research* **41,** 397–403.

McNevin D.B., Badger M.R., Whitney S.M., von Caemmerer S., Tcherkez G.G.B. & Farquhar G.D. (2007) Differences in carbon isotope discrimination of three variants of d-ribulose-1,5-bisphosphate carboxylase/oxygenase reflect differences in their catalytic mechanisms. *The Journal of Biological Chemistry* **282,** 36068–36076.

Marshall B. & Biscoe P.V. (1980) A model for C_3 leaves describing the dependence of net photosynthesis on irradiance. *Journal of Experimental Botany* **31,** 29–39.

Michelot A., Eglin T., Dufrene E., Lelarge-Trouverie C. & Damesin C. (2011) Comparison of seasonal variations in water-use efficiency calculated from the carbon isotope composition of tree rings and flux data in a temperate forest. *Plant, Cell & Environment* **34,** 230–244.

Montpied P., Granier A. & Dreyer E. (2009) Seasonal time-course of gradients of photosynthetic capacity and mesophyll conductance to CO_2 across a beech (*Fagus sylvatica* L.) canopy. *Journal of Experimental Botany* **60,** 2407–2418.

Ogée J., Peylin P., Ciais P., Bariac T., Brunet Y., Berbigier P., . . . Bonnefond J.M. (2003) Partitioning net ecosystem carbon exchange into net assimilation and respiration using $^{13}CO_2$ measurements: a cost-effective sampling strategy. *Global Biogeochemical Cycles* **17,** 1070–1088.

Ogée J., Barbour M.M., Wingate L., Bert D., Bosc A., Stievenard M., . . . Dewar R.C. (2009) A single-substrate model to interpret intra-annual stable isotope signals in tree-ring cellulose. *Plant, Cell and Environment* **32,** 1071–1090.

Parkinson K.J. (1971) Carbon dioxide infra-red gas analysis: effects of water vapour. *Journal of Experimental Botany* **22,** 169–176.

Pons T.L., Flexas J., von Caemmerer S., Evans J.R., Genty B., Ribas-Carbo M. & Brugnoli E. (2009) Estimating mesophyll conductance to CO_2: methodology, potential errors, and recommendations. *Journal of Experimental Botany* **60,** 2217–2234.

R Development Core Team (2009) *R: A Language and Environment for Statistical Computing*. R Foundation for Statistical Computing, Vienna, Austria. ISBN 3-900051-07-0, (URL: http://www.R-project.org).

Randerson J.T. (2002) A possible global covariance between terrestrial gross primary production and ^{13}C discrimination: consequences for the atmospheric ^{13}C budget and its response to ENSO. *Global Biogeochemical Cycles* **16,** 1136–1152.

Roeske C.A. & O'Leary M.H. (1984) Carbon isotope effects on the enzyme-catalyzed carboxylation of ribulose bisphosphate. *Biochemistry* **23,** 6275–6284.

Schoups G. & Vrugt J.A. (2010) A formal likelihood function for parameter and predictive inference of hydrologic models with correlated, heteroscedastic, and non-Gaussian errors. *Water Resources Research* **46,** 10531–10548.

Seibt U., Wingate L. & Berry J.A. (2007) Nocturnal stomatal conductance effects on the $\delta^{18}O$ signatures of foliage gas exchange observed in two forest ecosystems. *Tree Physiology* **27,** 585–595.

Sturm P. & Knohl A. (2010) Water vapor δ^2H and $\delta^{18}O$ measurements using off-axis integrated cavity output spectroscopy. *Atmospheric Measurement Techniques*, **3,** 67–77.

Sturm P., Eugster W. & Knohl A. (2012) Eddy covariance measurements of CO_2 isotopologues with a quantum cascade laser absorption spectrometer. *Agricultural and Forest Meteorology* **152,** 73–82.

Suits N.S. (2005) Simulation of carbon isotope discrimination of the terrestrial biosphere. *Global Biogeochemical Cycles* **19,** GB1017.

Taylor J.R. (1997) *An Introduction to Error Analysis: The Study of Uncertainties in Physical Measurements*, 2nd edn, University Science Books, Sausalito, CA, USA.

Tazoe Y., von Caemmerer S., Estavillo G.M. & Evans J.R. (2011) Using tunable diode laser spectroscopy to measure carbon isotope discrimination and mesophyll conductance to CO_2 diffusion dynamically at different CO_2 concentrations. *Plant, Cell and Environment* **34,** 580–591.

Tcherkez G. (2006) How large is the carbon isotope fractionation of the photorespiratory enzyme glycine decarboxylase? *Functional Plant Biology* **33,** 911–920.

Tcherkez G., Cornic G., Bligny R., Gout E. & Ghashghaie J. (2005) In vivo respiratory metabolism of illuminated leaves. *Plant Physiology* **138,** 1596–1606.

Tcherkez G., Schaeufele R., Nogues S., Piel C., Boom A., Lanigan G., . . . Ghashghaie J. (2010) On the $^{13}C/^{12}C$ isotopic signal of day and night respiration at the mesocosm level. *Plant, Cell and Environment* **33,** 900–913.

Tcherkez G., Mahe A. & Hodges M. (2011a) $^{12}C/^{13}C$ fractionations in plant primary metabolism. *Trends in Plant Science* **16,** 499–506.

Tcherkez G., Mauve C., Lamothe M., Le Bras C. & Grapin A. (2011b) The $^{13}C/^{12}C$ isotopic signal of day-respired CO_2 in variegated leaves of *Pelargonium x hortorum*. *Plant, Cell and Environment* **34,** 270–283.

Ubierna N. & Marshall J.D. (2011) Estimation of canopy average mesophyll conductance using $\delta^{13}C$ of phloem contents. *Plant, Cell & Environment* **34,** 1521–1535.

Van Oijen M., Rougier J. & Smith R. (2005) Bayesian calibration of process-based forest models: bridging the gap between models and data. *Tree Physiology* **25,** 915–927.

Vrugt J.A., ter Braak C.J.F., Diks C.G.H., Robinson B.A., Hyman J.M. & Higdon D. (2009) Accelerating *Markov Chain Monte Carlo* simulation by differential evolution with self-adaptive randomized subspace sampling. *International Journal of Nonlinear Sciences and Numerical Simulation* **10,** 273–290.

Warren C., Low M., Matyssek R. & Tausz M. (2007) Internal conductance to CO_2 transfer of adult *Fagus sylvatica*: variation between sun and shade leaves and due to free-air ozone fumigation. *Environmental and Experimental Botany* **59,** 130–138.

Warren C.R. (2008) Does growth temperature affect the temperature responses of photosynthesis and internal conductance to CO_2? A test with *Eucalyptus regnans*. *Tree Physiology* **28,** 11–19.

Warren C.R. & Dreyer E. (2006) Temperature response of photosynthesis and internal conductance to CO2: results from two independent approaches. *Journal of Experimental Botany* **57,** 3057–3067.

Werner C. & Gessler A. (2011) Diel variations in the carbon isotope composition of respired CO_2 and associated carbon sources: a review of dynamics and mechanisms. *Biogeosciences* **8,** 2437–2459.

Werner C., Schnyder H., Cuntz M., Keitel C., Zeeman M.J., Dawson T.E., . . . Gessler A. (2012) Progress and challenges in using stable isotopes to trace plant carbon and water relations across scales. *Biogeosciences* **9,** 3083–3111.

Whitehead D., Barbour M.M., Griffin K.L., Turnbull M.H. & Tissue D.T. (2011) Effects of leaf age and tree size on stomatal and mesophyll limitations to

photosynthesis in mountain beech (*Nothofagus solandrii* var. *cliffortiodes*). *Tree Physiology* **31,** 985–996.
Wingate L., Seibt U., Moncrieff J.B., Jarvis P.G. & Lloyd J.O.N. (2007) Variations in ^{13}C discrimination during CO_2 exchange by *Picea sitchensis* branches in the field. *Plant, Cell & Environment* **30,** 600–616.
Wingate L., Ogée J., Burlett R., Bosc A., Devaux M., Grace J., . . . Gessler A. (2010) Photosynthetic carbon isotope discrimination and its relationship to the carbon isotope signals of stem, soil and ecosystem respiration. *The New Phytologist* **188,** 576–589.
Zobitz J.M., Burns S.P., Reichstein M. & Bowling D.R. (2008) Partitioning net ecosystem carbon exchange and the carbon isotopic disequilibrium in a subalpine forest. *Global Change Biology* **14,** 1785–1800.

Received 3 April 2013; received in revised form 5 November 2013; accepted for publication 4 December 2013

SUPPORTING INFORMATION

Additional Supporting Information may be found in the online version of this article at the publisher's web-site:

Figure S1. Comparison of model residual analyses versus the leaf-to-air vapour pressure deficit (e_i–e_a) for the $^{13}\Delta_{comp}$ model with and without (Eqn 3) ternary corrections (Eqn A15), both for the $g_{s,obs}$ and the $g_{s,mod}$ approach. Values were calculated with MLE shown in Table 2 (Eqn 3, $g_{s,obs}$), Supporting Information Tables S1 (Eqn 3, $g_{s,mod}$) and S3 (Eqn A15, $g_{s,obs}$ and $g_{s,mod}$). Symbols denote the three different branch bags: BB1 – solid grey circles, BB2 – solid black triangles, BB3 – open black squares.

Figure S2. Predicted ($^{13}\Delta_{simple}$) versus observed ($^{13}\Delta_{obs}$) branch ^{13}C discrimination for the simplified model ($^{13}\Delta_{simple}$). All data points used for the respective modelling approach ($g_{s,obs}$ and $g_{s,mod}$) are shown. Model performance parameters can be found in Table 2 ($g_{s,mod}$) and Supporting Information Table S1 ($g_{s,obs}$).

Figure S3. Predicted ($^{13}\Delta_{comp}$) versus observed ($^{13}\Delta_{obs}$) branch ^{13}C discrimination for the comprehensive model ($^{13}\Delta_{comp}$). All data points used for the respective modelling approach ($g_{s,obs}$ and $g_{s,mod}$) are shown. Model performance parameters can be found in Table 2 ($g_{s,mod}$) and Supporting Information Table S1 ($g_{s,obs}$).

Figures S4 to S13. Observed and predicted $^{13}\Delta$ for all days of the 2010 field campaign. Time axis unit is hour in CET. Symbol error bars represent ± one propagated SD for the particular $^{13}\Delta_{obs}$ measurement. $^{13}\Delta_{obs}$ included in the *g*s,mod model calibrations are shown as closed black symbols, while those not included (for various reasons) are shown as open symbols.

Table S1. Summary of the $^{13}\Delta_{simple}$, $^{13}\Delta_{comp}$ model calibration inputs and outputs as well as model performance measures for the $g_{s,obs}$ approach. PM = estimated parameters; BB = branch bag; MLE = maximum likelihood estimate; P 2.5 and P 97.5 = 2.5 and 97.5 percentiles for posterior parameter distributions; Int. = intercept; max ln L = maximum of the natural logarithm of the negative likelihood; RMSE = root mean squared error. Slopes and intercepts were calculated using standard major axis – regression (SMA, model2 – regession); r^2 was calculated with ordinary least square regression. Unit for g_i is mol m^{-2} s^{-1}; all other parameters expressed in ‰.

Table S2. Correlation matrix of the calibrated model parameters of $^{13}\Delta_{comp}$ for the $g_{s,obs}$ approach. Prior parameter uncertainty ranges are identical to Supporting Information Table S1. Correlations are evaluated during repeated sampling from the posterior probability space and expressed by R values.

Table S3. Summary of the $^{13}\Delta_{comp,ternary}$ model calibration inputs and outputs as well as model performance measures for the both $g_{s,obs}$ and $g_{s,mod}$ approaches. PM = estimated parameters; BB = branch bag; MLE = maximum likelihood estimate; P 2.5 and P 97.5 = 2.5 and 97.5 percentiles for posterior parameter distributions; Int. = intercept; max ln L = maximum of the natural logarithm of the negative likelihood; RMSE = root mean squared error. Slopes and intercepts were calculated using standard major axis – regression (SMA, model2 – regession); r^2 was calculated with ordinary least square regression. Unit for g_i is mol m^{-2} s^{-1}; all other parameters expressed in ‰.

Table S4. Correlation matrix of the calibrated model parameters of $^{13}\Delta_{comp}$ for the $^{13}\Delta_{comp,ternary}$ approach. Prior parameter uncertainty ranges are identical to Supporting Information Table S3. Correlations are evaluated during repeated sampling from the posterior probability space and expressed by R values. Shaded = $g_{s,mod}$ and white = $g_{s,obs}$.

Table S5. Summary of the $^{13}\Delta_{comp,gi}{}^{25}$ model calibration inputs and outputs as well as model performance measures for the both $g_{s,obs}$ and $g_{s,mod}$ approaches. PM = estimated parameters; BB = branch bag; MLE = maximum likelihood estimate; P 2.5 and P 97.5 = 2.5 and 97.5 percentiles for posterior parameter distributions; Int. = intercept; max ln L = maximum of the natural logarithm of the negative likelihood; RMSE = root mean squared error. Slopes and intercepts were calculated using standard major axis – regression (SMA, model2 – regession); r^2 was calculated with ordinary least square regression. Unit for g_i is mol m^{-2} s^{-1}; all other parameters expressed in ‰.

Table S6. Correlation matrix of the calibrated model parameters of $^{13}\Delta_{comp}$ for the $^{13}\Delta_{comp,gi}{}^{25}$ approach. Prior parameter uncertainty ranges are identical to Table S5 Correlations are evaluated during repeated sampling from the posterior probability space and expressed by R values. Shaded = $g_{s,mod}$ and white = $g_{s,obs}$.

Table S7. Summary of the $^{13}\Delta_{comp,ternary,gi}{}^{25}$ model calibration inputs and outputs as well as model performance measures for the both $g_{s,obs}$ and $g_{s,mod}$ approaches. PM = estimated parameters; BB = branch bag; MLE = maximum likelihood estimate; P 2.5 and P 97.5 = 2.5 and 97.5 percentiles for posterior parameter distributions; Int. = intercept; max ln L = maximum of the natural logarithm of the negative likelihood; RMSE = root mean squared error. Slopes and intercepts were calculated using standard major axis – regression (SMA, model2 – regession); r^2 was calculated with ordinary least square regression. Unit for g_i is mol m^{-2} s^{-1}; all other parameters expressed in ‰.

Table S8. Correlation matrix of the calibrated model parameters of $^{13}\Delta_{comp}$ for the $^{13}\Delta_{comp,ternary,gi}{}^{25}$ approach. Prior parameter uncertainty ranges are identical to Table S7. Correlations are evaluated during repeated sampling from the posterior probability space and expressed by R values. Shaded = $g_{s,mod}$ and white = $g_{s,obs}$.

APPENDIX

General isotope terminology

Carbon isotope ratios are given in the δ notation (expressed in ‰), that is defined as the relative difference in the molar $^{13}C/^{12}C$ ratios of a measured sample (R_{sample}) and the international reference standard Vienna Pee Dee Belemnite ($R_{V\text{-}PDB}$):

$$\delta^{13}C = \frac{R_{sample} - R_{V-PDB}}{R_{V-PDB}} \quad (A1)$$

The carbon isotope discrimination by a plant was defined as (Farquhar & Richards 1984)

$$^{13}\Delta_{plant} = \frac{R_{air} - R_{plant}}{R_{plant}} = \frac{\delta_{air} - \delta_{plant}}{1 + \delta_{plant}} \quad (A2)$$

Calculation of gas exchange parameters

As *Fagus sylvatica* leaves are hypostomatous, all measures are expressed in terms of unit leaf area (L) for one side of the leaves only (one-sided).

The rate of transpiration E per unit leaf area L was calculated following von Caemmerer & Farquhar (1981) as

$$E = \frac{f}{L}\frac{(w_o - w_e)}{(1 - w_o)} \quad (A3)$$

where f is the molar flow rate of moist air entering the branch bag, calculated from a volume flow rate ($dm^3\ min^{-1}$) by application of the ideal gas law using temperature and pressure measured at the site, and w_e and w_o are the mole fractions of water vapour at the branch bag inlets (ambient air) and outlets (chamber air).

The rate of the net CO_2 assimilation during daytime A_n (PAR > 10 μmol $m^{-2}\ s^{-1}$) includes both leaf and twig net CO_2 fluxes of enclosed beech branches and was calculated per unit leaf area L as

$$A_n = \frac{\phi}{L}(c_e - c_o) \quad (A4)$$

where c_e and c_o are the CO_2 mole fractions of dry air at the branch bag inlets and outlets. Air was dried with a membrane drier (PD-200T-24 Perma Pure LLC, ansyco GmbH, Karlsruhe, Germany), before entering the QCLAS–ISO. Since the FEP film, covering the branch bag construction frame, was fastened in a flexible manner, air pressure within and outside the bags was assumed to be equal. The flow rate on the outlet was not corrected for any increase in moisture generated by transpiration in the branch bag (Parkinson 1971) and thus assumed equal to the flow rate of moist air on the inlet ϕ ($dm^3\ min^{-1}$).

The CO_2 mole fraction of chamber air $c_{a,}$ used for $^{13}\Delta$ predictions, was assumed to be equal to c_o and no corrections were made for water vapour dilution of chamber air, for the reasons given above for A_n.

The flux-weighted daily mean of $^{13}\Delta_{obs}$ was calculated as

$$\overline{^{13}\Delta_{obs,D}} = \frac{\sum_{k=1}^{N} {}^{13}\Delta_{obs,k} A_{n,k}}{\sum_{k=1}^{N} A_{n,k}} \quad (A5)$$

where N is the number of daytime measurements for a particular day (defined as PAR > 10 μmol $m^{-2}\ s^{-1}$). The same equation was used for modelled values, and observed and modelled flux-weighted daily means were always calculated for identical N and k in Eqn A5. Days with an insufficient N or a time of day bias were excluded from the analysis.

Saturation water vapour pressure (e_{sat}) was calculated based on Buck (1981):

$$e_{sat} = 0.61364 \exp\left(\frac{17.502T}{240.97 + T}\right) \quad (A6)$$

with e_{sat} in kPa, and T defined as air or lower leaf surface temperature in °C, either measured inside or outside the branch bag depending on the application.

Relative humidity (h) was calculated using the following relationships:

$$e = w\ p_{atm} \quad \text{and} \quad h = \frac{e}{e_{sat}} \quad (A7–A8)$$

where w denotes water vapour mole fractions and e denotes water vapour pressures of either ambient or branch bag air, and p_{atm} is the atmospheric pressure at the site.

Observed stomatal conductance ($g_{s,\ obs}$) was calculated as

$$w_i = \frac{e_{sat,T_{Leaf}}}{p_{atm}} \quad (A9)$$

$$g_{tw} = \frac{E}{w_i - w_o} \quad (A10)$$

$$\frac{1}{g_s} = \frac{1}{g_t} - \frac{1}{g_b} \quad \text{with} \quad g_{sc} = \frac{g_{sw}}{1.6} \text{ and } g_{bc} = \frac{g_{bw}}{1.37} \quad (A11–A13)$$

where g denotes conductance; w_i is the T_{Leaf}-derived mole fraction of water vapour inside the leaf, assuming water vapour saturation inside leaves; T_{Leaf} is the lower leaf surface temperature within the branch bags; the first subscript t, s, b denotes total, stomatal and boundary-layer conductance, respectively; the second subscript w and c denotes conductances for water vapour and CO_2. No ternary correction (Jarman 1974; von Caemmerer & Farquhar 1981) was applied to Eqn A10.

Alternative equations using ternary corrections

Ternary corrections in gas exchange equations account for effects that collisions between molecules in a ternary system of gases – CO_2, water vapour and air – have on the diffusive flux of CO_2 and water vapour through the stomatal pore (Jarman 1974; von Caemmerer & Farquhar 1981). Given the probable measurement imprecisions arising from stomatal heterogeneity or from volume flow rate and leaf area determinations, we first neglected ternary effect corrections to Eqn A10 (g_{tw}) and Eqn 6 (c_i) and for consistency, ternary corrections were also not applied to Eqns 3, 4 and 5 (Farquhar & Cernusak 2012). Nonetheless, we tested the influence of ternary effect corrections on model calibration and behaviour of $^{13}\Delta_{comp}$ (Eqn 3) by incorporating such corrections into Eqns 3 and 6. Equation A10 was not changed in order to preserve the original input dataset but including the ternary correction into Eqn A10 would have lowered $g_{s,obs}$ values by less than 4%.

When accounting for ternary effects, the calculation for c_i given in Eqn 6 changes to Eqn A14 (von Caemmerer & Farquhar 1981):

$$c_{i,TERN} = \frac{\left(g_{tc} - \frac{E}{2}\right) c_a - A_n}{\left(g_{tc} + \frac{E}{2}\right)} \tag{A14}$$

and the model formulation for $^{13}\Delta_{comp}$ given in Eqn 3 changes to Eqn A15 (Farquhar & Cernusak 2012):

$$^{13}\Delta_{comp,TERN} = \frac{1}{1-t}\left[a_b \frac{c_a - c_s}{c_a} + a \frac{c_s - c_i}{c_a}\right] + \frac{1+t}{1-t}\left[(e_s + a_l)\frac{c_i - c_c}{c_a} + b\frac{c_c}{c_a} - \frac{\alpha_b}{\alpha_f} f \frac{\Gamma^*}{c_a} - \frac{\alpha_b}{\alpha_e} e \frac{R_{day}}{A_n + R_{day}} \frac{c_c - \Gamma^*}{c_a}\right] \tag{A15}$$

with $= \frac{\alpha_{ac} E}{2\, g_{tc}}$, $\alpha_{ac} = 1 + \bar{a}$, $\bar{a} = a_b \frac{c_a - c_s}{c_a - c_i} + a \frac{c_s - c_i}{c_a - c_i}$, $\alpha_b = 1 + b$, $\alpha_f = 1 + f$ and $\alpha_e = 1 + e$.